Numerical modeling of varying hemodynamic features with changing internal carotid artery bifurcation angles and degrees of stenosis.

AL BISHTAWI, B., SOO, Y.H., CHAN, A.T.Y. and SCRIBANO, G.

2023

Numerical Modelling of Varying Hemodynamic Features with Changing Internal Carotid Artery Bifurcation Angles and Degrees of Stenosis

Basel Al Bishtawi[1], Yan Hao Soo[1], Andy Chan Tak Yee[1] and Gianfranco Scribano[1,a)]

[1]*Department of Mechanical, Materials, and Manufacturing Engineering, Faculty of Science and Engineering,*

University of Nottingham Malaysia, 43500 Semenyih, Selangor, Malaysia

[a)]*Authors to whom correspondence should be addressed. Electronic mail: gianfranco.scribano@nottingham.edu.my.*

Atherosclerosis is a disease clinically categorized as a silent killer as its symptoms only become pronounced after the buildup has extensively progressed. Therefore, early detection, prediction and treatment become of great priority. The focus of this study is to develop a deeper understanding of plaque formation and the role of key structural variations, specifically the bifurcation angle and degree of stenosis, on its progression in a numerical carotid artery model. A two-way coupled Fluid-Solid Interaction (FSI) numerical approach has been implemented, with the consideration of isotropic elasticity for the artery wall. Geometrically induced hemodynamic flow variations were monitored by tracking changes in hemodynamic indicators, such as the wall shear stress (WSS) and vortex structures. The numerical results demonstrate general trends of the bifurcation angle amplifying recirculation zones, reducing WSS at the sinus far walls, and inhibiting wall deformations about the apex. Meanwhile, progressive stenosis is shown to induce new vortices, increase and decrease WSS at the outer walls and the inner walls respectively, and promote larger deformations. These hemodynamic flow and structural variations hint at increased risk of further plaque buildup with the increase of bifurcation angle at lower degrees of stenosis, while an increased risk of plaque rupture was associated with higher degrees of stenosis.

1. Introduction

In medicine, cardiovascular disease (CVD) is an umbrella term that lumps heart-related diseases including, but not limited to, cerebrovascular accident (CVA) [1], chronic obstructive pulmonary disease[2], and coronary heart disease [3]. Such diseases are considered to be the leading cause of non-communicable disease (NCD) mortality worldwide, with an estimated 17.9 million recorded deaths according to the World Health Organization (WHO)'s 2019 CVDs report [4]. As cardiovascular diseases generally refer to anomalies in blood flow patterns to the intended organs, their causes typically intertwine with one another. For instance, CVA, otherwise known as a stroke, is categorized into two groups, namely ischemic and hemorrhagic. An ischemic stroke simply refers to a decreased blood flow to the brain due to a blood clot [5]. Meanwhile, a hemorrhagic stroke defines a stroke due to the weakening and rupture of arteries, which is followed by blood leakage into the intracranial cavity [6]. However, the two types can coincide in occurrence, where the blood clot can induce an artery rupture and lead to this leakage [7]. Therefore, this highlights the importance of closely scrutinizing the occurrence

of blood clots and its factors. According to Qiu et al. [8], uncontrolled blood clotting during atherosclerosis can occur due to the rupturing of the plaque build-up in the artery. Hence, in such scenarios, the risk of a weakened, ruptured artery becomes significantly higher.

Typically, atherosclerotic plaque occurs preferentially at complex anatomical sites such as bifurcations, junctions, and bends where the hemodynamic stability at those locations is susceptible to geometric variation [9,10]. The localization of atherosclerotic plaque is most pronounced at the widened segment of ICA, commonly referred as carotid sinus where it contains baroreceptors which are responsible for blood pressure detection and regulation [10,11]. From a hemodynamic point of view, it is widely accepted that locally disturbed flow patterns characterized by low and oscillating WSS plays a more significant role in the initiation and development of atherosclerotic plaque compared to high wall shear stress (WSS) [12-14]. The earliest discovery of such correlation can be backdated to late 60's and early 70's where Caro et al. [15,16] indicated that the formation of atherosclerotic lesions was linked to regions with low WSS. The low WSS theory has been backed by numerous researchers [10,11,17,18] and has been widely adopted since then.

In classical medicine, the plaque deposition size has been, and still is, a primary indicator of stenosis severity. Thus, it acts as a deterministic factor of the type of therapeutic procedure that needs to be undertaken by the patient. Currently, both the North American Symptomatic Carotid Endarterectomy Trial (NASCET) and the European Carotid Surgery Trial (ECST) criteria are recognized as criteria that enable the prediction and prevention of a potential stroke due to an existing carotid artery stenosis [19]. However, significant differences lay in their calculations and categorizing of stenosis degrees. In the case of NASCET, the stenosis percentage is calculated as the diameter difference between the internal carotid artery (ICA) and its stenosed section. Moreover, NASCET assumes a stenosis percentage of $\geq 70\%$ requires endarterectomy. Meanwhile, ECST calculates the stenosis by finding the difference between the original diameter of the stenosed section and its reduced diameter due to stenosis. Unlike NASCET, ECST assumes a stenosis percentage $\geq 80\%$ requires an endarterectomy. Many comparative investigations attempted finding a deterministic conclusion as to which criterion is precise quantification of the stenosis degree. Studies such as Staikov et al. [20], Donnan et al. [21], and Rothwell et al. [22] all have unanimously concluded that the NASCET method tends to underpredict the degree of stenosis when compared to the ECST method. However, Saba et al.[23] have determined that this difference between the two methods gradually becomes insignificant. While the two methods have their differences, they share the same shortcomings when it comes to predicting the severity of eccentric stenosis. Many studies have observed an increased stroke vulnerability in patients experiencing an eccentric stenosis [24]. Therefore, it is essential to understand physiological cause and effect of such kind of stenosis.

In fact, numerous studies have been conducted by researchers in the past to investigate the hemodynamic effect of bifurcation angle variation in arteries. Considerable number of numerical studies have been performed using idealized and patient specific geometries to investigate the hemodynamic effect of bifurcation angle variation in healthy carotid arteries. Similar findings were obtained where reduction of flow velocity and wall shear stress, accompanied with enhanced flow separation and recirculation, occurs prominently at the outer carotid sinus wall with increasing bifurcation angles [25-27]. On the other hand, extensive research works have been done to study the hemodynamic influence of bifurcation angle variation in coronary arteries under both healthy and pathological conditions, Chaichana et al. [28] and Rabbi et al. [29] investigated how angle variation effects hemodynamic behavior of idealized and patient-specific coronary artery models with bifurcation geometries. The results from both studies agree with the findings from carotid bifurcation explorations in which reduction of velocity magnitude and wall shear stress increases with angulation. From another point of view, Liu et al.[30] employed computational fluid dynamics (CFD) to quantify the effects of curvature and bifurcation on blood flow dynamics in coronary arteries. Their findings disagreed with Chaichana et al. [28] and Rabbi et al.[29] indicating that the low WSS regions witness a reduction with the increase of the branch angle.

Various arguments regarding the influence of bifurcation angle on the development of atherosclerotic lesions exist, but no definitive conclusion has been reached on the question of which or whether if bifurcation angles favor its formation. For instance, Friedman et al. [31] investigated the relationship between bifurcation angle of left main coronary artery and the distribution of early sudanophilic lesions and their findings contradicted with the results from Perktold et al. [18], Nguyen et al. [27], and Saho et al. [26], indicating that hemodynamic disturbance are more prominent in lower level bifurcation (small angle). On the other hand, Chiastra et al. [32] evaluated the hemodynamic effects the bifurcation angle and curvature radius variations have in both healthy and stenosed coronary arteries. The results showed that the bifurcation angle has negligible effects on the hemodynamics in both healthy and stenosed arteries as compared to the effects of the curvature radius. Decreasing the radius was shown to catalyze formations of helical fluid structures; however, it presented moderate effects on near-wall wall shear stress in stenosed cases. Meanwhile, the reduction of areas with low time-averaged wall shear stress was primarily more pronounced in healthy models with larger bifurcation angles, confirming previous investigations [28,30,33]. Similarly, Lee et al. [34] quantified the relationship between various geometric factors and hemodynamic disturbances including bifurcation angle and concluded that there is no significant association between bifurcation angle and flow disturbance.

Apart from bifurcation geometry, the assumption of rheological properties of blood remains controversial until today as there were various arguments on the question of whether blood is of Newtonian or non-Newtonian nature. The adoption of Newtonian model for blood is reasonable due to the fact that non-Newtonian characteristics of the blood has negligible effect on the hemodynamic parameters [10,17,18]. However, Gijsen et al. [35] and Chen et al. [36] reported a significant difference in results, when a non-Newtonian model was employed in a steady bifurcation. Newtonian approximation is acceptable for large vessels (such as carotid artery) as the shear rates are higher than 100 s^{-1} [37] and the size of blood cells is small compared to the vessel diameter[38].

On another note, the effect of inlet flow velocity on hemodynamics was yet another hemodynamic property investigated in numerous studies [39-43] with majority of the studies [41-43] indicating that the modification in the inlet velocity did not produce changes in the wall shear stress as significant as what geometric variation would produce. For instance, Moyle et al.[41] quantified the solution errors imposed by the substitution of 3D in vivo velocity profile with Womersley profile and has discovered that the geometric variation induced more influence over the WSS than variations in inlet velocity profiles. The findings were supported by Campbell et al. [42] which studied the effects of employing different idealized inlet velocity profiles (flat, parabolic and Womersley) by comparing mean WSS with simulation employing patient-specific velocity profile. It was discovered that all simulations exhibited remarkably similar result in terms of wall shear stress distribution and magnitude regardless of the inlet velocity profile shape with geometrical variation imposing more significant changes compared to the choice of inlet velocity profile. While the statements may hold true in the studies' respective geometries, it is important to consider that such conclusion does not hold in cases where the velocity profile cannot be assumed symmetrical. In other words, this 'a priori' approach is unreliable in cases where the flow is fully developed in the carotid artery [44]. In reality, the velocity profile is known to be influenced by many factors, namely pulsatility, viscosity, diameter of vascular regions, and more recently the severity of stenosis [45]. Furthermore, case studies observing the flow at regions near the aorta or about the carotid siphon will face challenges implementing the said velocity profiles as numerical predictions of the flow [46]. This is because the flow is generally not fully developed yet, making it an inaccurate prediction. As for the majority of the studies that study the carotid artery near the sinus, velocity profiles such as the Womersley profile [40] are deemed closer to realistic blood flow profiles.

Surely, many investigations found in the literature had the tendency to numerically investigate patient-specific healthy and stenosed carotid artery models alike to scrutinize underlying hemodynamic behaviours in those specific models and their relation to atherosclerosis development. While these studies uncover a multitude of relationships between the blood rheology

with arterial wall behaviour and the development of atherosclerosis, these studies are typically restricted to one geometry. This limitation sources from the fact that carotid arteries vary from one person to another, in addition to its interpersonal variation. This deems it a challenge to generalize the deduced conclusions from these studies. Therefore, as a simplistic workaround to this problem, this investigation considers an idealized model of the carotid artery that enables a modular variation to the artery geometry through changing the bifurcation angle and the degree of stenosis. Moreover, a fluid-solid interaction (FSI) method is implemented in the investigation to highlight the impact of the induced hemodynamics by the geometrical manipulations on the artery wall. This study presents a comprehensive analysis of the hemodynamic effect of bifurcation angle variations and stenosis severities will be presented in the following sections of this report. The report is dissected into the following: (i) Section II discusses the fluid and static modelling methodology used in setting up the numerical simulation (ii) Section III presents and elaborates on the numerical results describing key hemodynamic parameters, such as flow velocity and the wall shear stress (WSS) (iii) Section IV draws key conclusions from the analysed data.

2. Numerical methodology

2.1. Carotid artery geometry and case setup

In this numerical investigation, 12 three dimensional (3D) idealized carotid artery cases were constructed using ANSYS 2020 R2 Design Modeler. The idealized model simply refers to the assumption of a straight cylindrical pipe as the base modelling concept behind the formation of the carotid artery geometry. This is highlighted in the base carotid artery model shown in FIG 1 in which the model is composed of the fluid domain for blood flow and the structural domain for the artery wall. This form of modelling is employed to perform a fluid-structure interaction (FSI) simulation shown later in Sec II B. The base model is divided into three main parts, namely the common carotid artery (CCA), the internal carotid artery (ICA), and the external carotid artery (ECA), where the typical carotid geometrical features are introduced. A primary example is the carotid stenosis that lies at the beginning of the ICA past the artery junction. The dimensions of each of the carotid artery's features are summarized in Table 1. Moreover, in the cases shown in FIG 3, two key geometrical parameters were varied: the bifurcation angle and the degree of stenosis at the carotid sinus. These parameters were obtained from Perktold et al.[18] and Perktold et al.[25] and were considered in this investigation, as tabulated in Table 1.
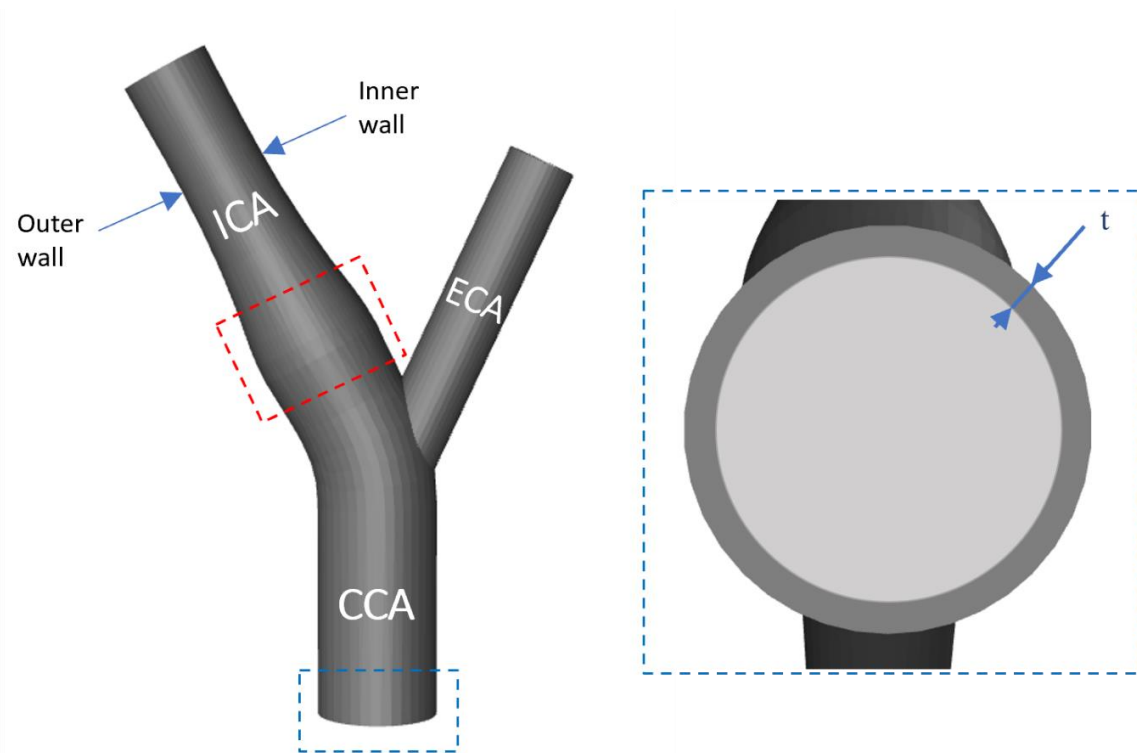
FIG. 1. Labelled schematic of the carotid artery bifurcation base geometry at a bifurcation angle of 50° where the CCA is the common carotid artery, ICA is the internal carotid artery, and the ECA is the external carotid artery. The ICA angle is 25°. The red dashed box highlights the carotid sinus region where stenosis is predicted to occur, while the blue dashed box represents the location of the zoomed sectional view of the CCA showing the modelling of the artery wall with respect to the fluid domain, where t is the wall thickness.

Furthermore, a notable dimensioning assumption is that the basis of the model construction is accounting for bifurcation angle changes through varying the internal carotid angle from 15° to 40° while maintaining the external carotid angle at 25°. The investigated values were obtained through cross-examination of previous patient-specific experimental studies and extracting a range that sits well within the mean range reported in those works. In particular, with the accounting of the common carotid artery centerlines, Thomas et al.[47] reported bifurcation angle of 61.5° ± 4.1°, Foster et al.[48] reported 56° ± 13° and Kamenskiy et al.[49] reported 47.77° ± 25.61°. As for the second geometric parameter, the degree of stenosis is varied with respect to the stenosis severity standardized by the European Carotid Surgery Trial (ECST) [50], as it was argued that this criterion showed linearity with the risk of ipsilateral cerebrovascular or retinal ischemic (CORI) events and allows for a linear conversion between different stenosis measurement methods [51,52]. Hence, in the artery geometry construction, ECST stenosis percentages of 0%, 50%, 70%, and 80% were modelled and chosen for exploration.
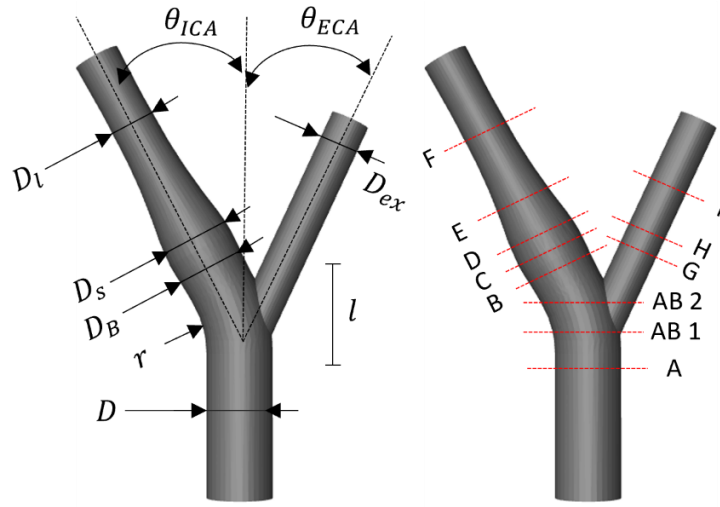
FIG. 2. Dimensioned base carotid artery model is shown on the left-hand side figure where the values of each parameter are summarized in Table 1. The right-hand side figure shows a series of section planes along the artery representing monitoring sites for the collection and processing of numerical data.

Table 1. Geometric parameters for the generation of the base carotid artery model shown in FIG 2.

Geometric Parameters	ICA Angle, θ_{ICA} (°)		
	15	25	40
Diameter of common carotid artery, D (mm)	6.2	6.2	6.2
Diameter of internal carotid artery, D_i (mm)	4.34	4.34	4.34
Diameter of external carotid artery, D_{ex} (mm)	3.658	3.658	3.658
Diameter of cross section at Level B, D_B (mm)	6.324	6.324	6.324
Maximum carotid sinus diameter, D_s (mm)	6.572	6.572	6.572
Radius of curvature, r_c (mm)	26.04	13.95	11.16
Distance of apex from Level A, l (mm)	7.44	7.13	7.13
Artery wall thickness, t (mm)	0.7	0.7	0.7

The labelling letters, A, B, C, D in FIG 2 illustrates different flow cross-section levels at which numerical results, such as contour plots, are collected and presented. Cross-section level A refers to the common carotid artery; AB 1 and AB 2 both capture the blood flow about the artery junction. Meanwhile, B, C, D, E, and F collectively represent the blood flow in the internal carotid where level B is proximal to the carotid sinus, level C coincides with the maximum sinus diameter, levels D and E are proximal to the carotid sinus downstream, while level F represents the flow at the nominal cross-sectional area of the internal carotid artery. On the other hand, planes G, H, and I model the flow within the external carotid artery. The

proximal section of ICA was revealed as one of the regions which is the most vulnerable to intimal thickening and plaque formation according to the quantitative determinations from Zarins et al.[10]. With the consideration of the aforementioned stenosis criteria, the stenosed carotid models were constructed by adapting an eccentric stenosis growth on the base carotid artery model at the proximal internal carotid artery sinus. An eccentric stenosis was chosen for modelling since it presents multiplied levels of severity compared to its size, as opposed to the typical concentric stenosis conditions. The eccentric stenosis was emulated in the geometry by assuming a semi-cylinder cutting through the outer wall of the carotid sinus. The semi-cylinder's

is adjusted to represent different degrees of stenosis, as per the definitions of stenosis severity provided by the ECST criterion. This criterion is mathematically defined as

$$\% \, ICA \, Stenosis = \frac{\emptyset_{ICA} - \emptyset_{Stenosis}}{\emptyset_{ICA}} \times 100 \tag{1}$$

Where $\emptyset_{ICA}$ is the original diameter at the site of stenosis, $\emptyset_{Stenosis}$ is the minimum diameter of the site after stenosis. Therefore, quantifying and assessing the artery's hemodynamics during such cases of stenosis becomes of great importance and concern. This stenosis shape was chosen as one of the many approximations of naturally occurring plaque buildup in patient-specific carotid arteries. Typically, these approximations are inspired by CT-scans and MRI-scans previously published of patient-specific stenosed arteries [53,54]. Freidoonimehr et al. [55] demonstrate the influence of different stenosis shapes have on the downstream flow behavior mentioning that the downstream velocity profiles do not vary heavily with different eccentric stenosis shapes. However, flow transitional behavior, coherent structures, and re-laminarization of downstream flow vary steeply from one shape to another. It has been demonstrated that the 'half-moon' eccentric stenosis, a term Freidoonimehr et al. [55] use to describe the semi-cylinder shape, induces higher flow fluctuations and higher pressure drops that hint at more serious hemodynamic complications with increased degree of stenosis. Therefore, the semi-cylindrical shape has been chosen for investigation to scrutinize its potential dangers with respect to variations in the bifurcation angle.

As for the carotid artery geometry, the assumption of a simplified carotid artery geometry was made to simplify the process of creating new iterations of the geometry by changing the bifurcation angle and the degree of stenosis. However, with this geometrical simplification, some geometrical attributes associated with real carotid artery models were neglected. Unlike the studied straight cylindrical geometry, typical patient-specific carotid artery geometry would illustrate small curvatures about each of the three main artery sectors, CCA, ICA, and the ECA. Moreover, patient-specific arteries tend to show some degree of cross-sectional eccentricity [56,57]. Generally, the key parameter that is dependent on such geometrical attributes is the velocity distribution. The presence of curvatures and eccentricities tend to induce eccentricity in the velocity

profile downstream of the CCA, ICA, and ECA. However, it has been shown in the literature that this deviation of the velocity profile is insignificant, specifically at the carotid sinus [58]. Therefore, the numerical analysis was carried out with the simplified model.
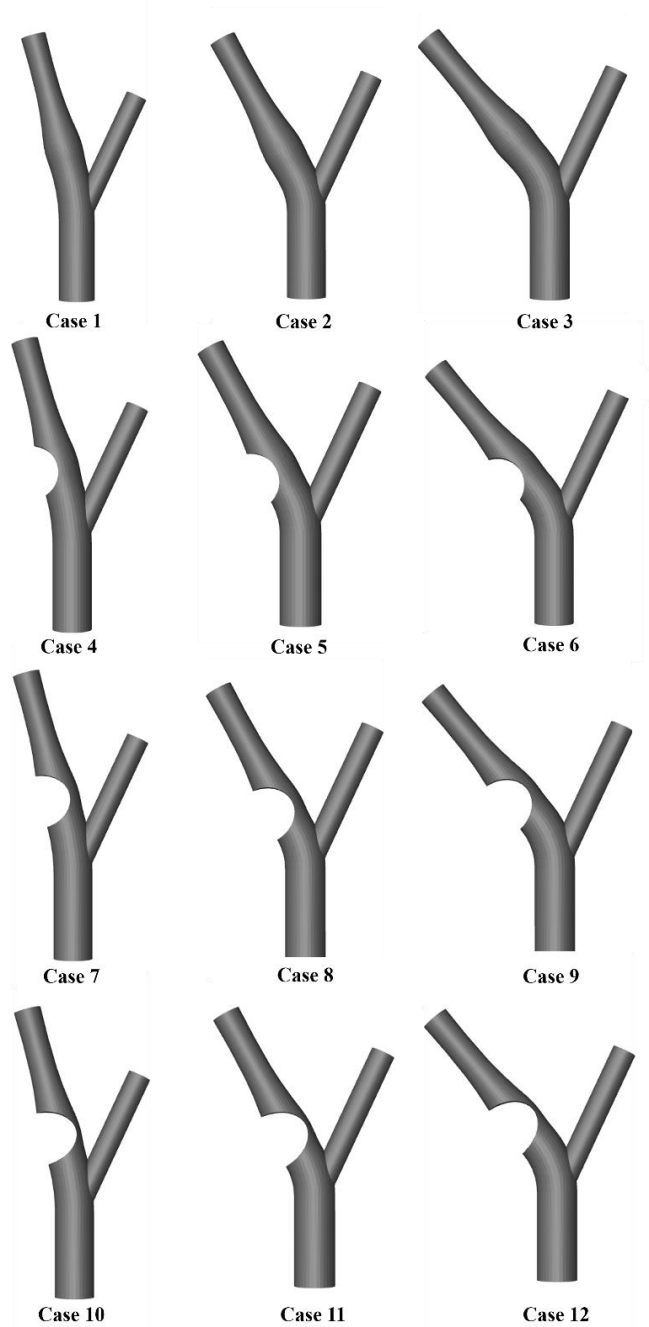
FIG. 3. The 12 cases of geometrical variations in the base model of the carotid artery's bifurcation angle and degree of eccentric stenosis at the carotid sinus. The diagram shows these variations applied on the fluid domain of the carotid artery to model the blood flow path within the carotid artery wall. The cases are summarized in a matrix presented in Table 2.

Table 2. Geometrical conditions of the carotid artery model for each case shown in FIG 3.

ECST Percentage of Stenosis	ICA Angle, $\theta_{ICA}(°)$		
	15	25	40
0%	Case 1	Case 2	Case 3
50%	Case 4	Case 5	Case 6
70%	Case 7	Case 8	Case 9
80%	Case 10	Case 11	Case 12

2.2. FSI governing equations

In this section, the set of equations that describe the blood flow, and its hemodynamic behavior, in the presented carotid artery models are identified and discussed. Typically, such equations govern the continuity and the momentum of the simulated fluid flow. In addition, these equations are generally coupled with a turbulence model that defines the turbulent attributes of flow by implementations of either Reynolds-averaged Navier Stokes (RANS) models or Large Eddy Simulations (LES) models. In other cases, Direct Numerical Simulation (DNS) is implemented to resolve the Navier-Stokes equation directly without the use of turbulence models [59]. However, in the case of the aforementioned carotid artery model, the blood flow is assumed laminar [60-62], and thus, no turbulence model is employed. Instead, an additional set of governing equations that describe the interaction between the arterial blood flow and the artery wall is considered; these equations fall under a numerical category known as fluid-structure interaction (FSI).

Generally, FSI is a numerical method that mediates between the CFD solver and the FEA solver that translates flow-induced force on a given structure to load on that structure, in which the structural displacement is then computed. This solver coupling is grouped as follows: one-way coupling and two-way coupling. As the names suggest, a one-way coupling simply means that the transfer of data occurs only in one direction from the fluid solver into the structural solver. More specifically, the force applied by the fluid is calculated and input into the structural solver to calculate the displacement. Similarly, the two-way coupling performs the same calculation; however, the calculated displacement is then fed back into the fluid solver to assess the effect of this structural deformation on the fluid flow. For this investigation, with the degree of fidelity required to model the complete arterial behavior, a two-way coupling is employed, as shown in FIG 4.
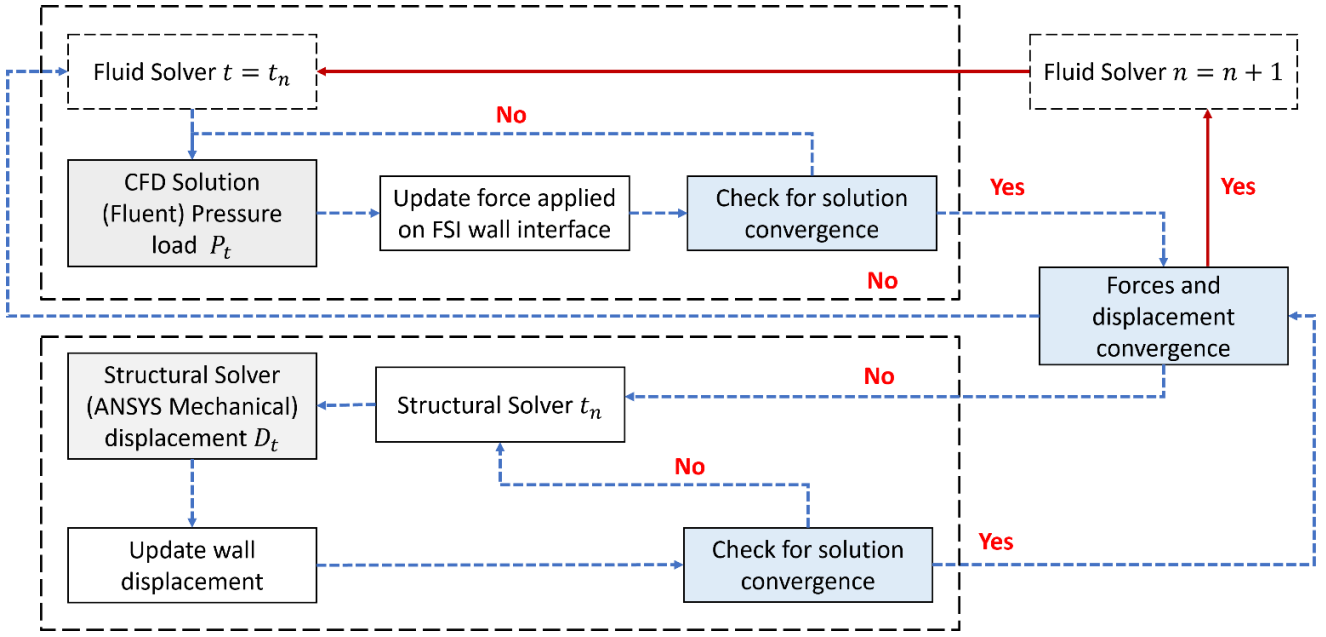
FIG. 4. FSI schematic of the two-way coupling between the CFD and Structural solvers.

2.3. Blood flow modelling

As mentioned earlier, the blood flow is assumed to be laminar, as the bulk Reynolds number attained in the artery is 921.14. Moreover, it is assumed to be incompressible, Newtonian, and pulsatile. These assumptions are found appropriate as it has been unanimously understood that the singular blood cell diameter is comparatively small compared to the artery's diameter[63]. Therefore, the blood's viscosity is assumed constant and independent from the shear rate. Accordingly, the equations that govern the flow in the numerical setup are then expressed and implemented as such:

$$\nabla \cdot \boldsymbol{u} = 0 \tag{2}$$

$$\rho_{\psi_f} \left(\frac{\partial \boldsymbol{u}}{\partial t} + (\boldsymbol{u} \cdot \nabla)\mathbf{u} \right) = -\nabla\mathrm{P} + \mu_{\psi_f} \nabla^2 \mathbf{u} \tag{3}$$

In which ρ_{ψ_f} represents the blood density, $\boldsymbol{u}$ is the velocity vector, P is the pressure, μ_{ψ_f} is the dynamic viscosity of blood, and lastly, t is the flowtime. Equation 2 defines the continuity where a mass flow balance is described to be maintained throughout the entire flow simulation. However, this highlights the assumption made in Equation 3 in which body forces, such as gravitation forces, are neglected.

2.4. Structural deformation

With the aforementioned setup of blood flow, it is understood that blood can generally exert some form of force in terms of pressure on the artery walls. Typically, when FSI is employed, one must decide the methodological approach, be it the

Lagrangian approach or the Eulerian approach. Therefore, a FSI approach utilizing the standard arbitrary Lagrange-Eulerian (ALE) method [64] is employed to acknowledge such force exertion and account for its consequent impact on the artery walls in terms of displacement and deformation. As a two-way coupling is utilized, this is performed in an iterative manner, where pressure profiles are passed from the fluid solver, represented by ANSYS Fluent 21[65][65][64][64][61], to the structural solver, represented by ANSYS Mechanical 21[66][66][65][65][62], and the calculated displacements are then cycled back from the structural solver to the fluid solver. This iterative process continues until a converged solution is reached and a global solution is achieved. Figure 5 below highlights the location at which the FSI method is implemented.
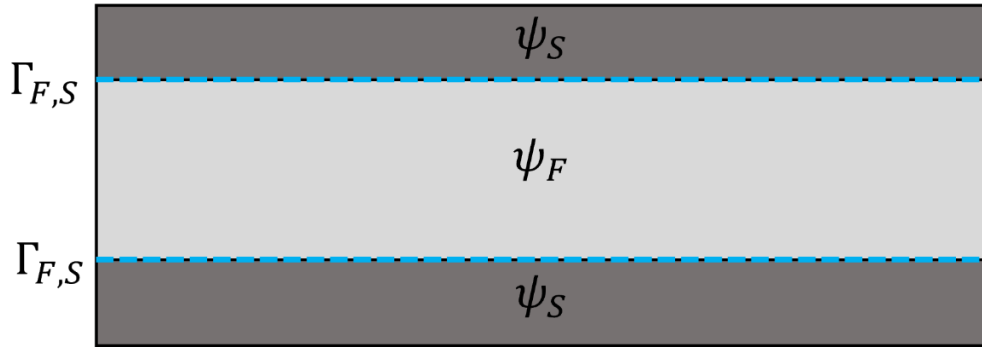
FIG. 5. FSI domains and the boundary interface at which the data transfers occur in the artery. ψ_S represents the solid artery wall domain, ψ_F represents the fluid blood domain, and $\Gamma_{F,S}$ highlights the boundary interface.

As the mathematical representations of the fluid domain are covered in Equations 2 and 3, the governing equations of the structural wall, specifically its deformations, are expressed by the linear momentum conservation equation written as follows:

$$\rho_{\psi_S} \frac{\partial^2 \boldsymbol{d}}{\partial t^2} - \nabla \cdot \overline{\overline{\sigma}} = \rho_{\psi_S} \boldsymbol{b} \tag{4}$$

Where ρ_{ψ_S} is the artery wall density, d is the wall displacement, $\boldsymbol{b}$ stands for the vector of body forces exerted on the wall, and $\overline{\overline{\sigma}}$ is the Cauchy stress tensor [67] where it equates to:

$$\overline{\overline{\sigma}} = 2\mu_L \overline{\overline{\varepsilon}} + \lambda_L \, tr(\overline{\overline{\varepsilon}}) \, I \tag{5}$$

I is an identity matrix, $\overline{\overline{\varepsilon}}$ is the infinitesimal strain tensor, tr is the trace function, while λ_L and μ_L represent the first and second Lamé parameters. These parameters are expressed as shown in Equations 6 and 7. It is important to keep in mind that Equation 5 holds true only when the artery wall is assumed to behave in a homogeneous isotropic, linear, and elastic manner [68].

$$\lambda_L = \frac{\nu E}{(1+\nu)(2\nu-1)} \tag{6}$$

$$\mu_L = \frac{E}{2(1+\nu)} \tag{7}$$

Moreover, for the FSI setup to establish a coupling between the mathematical models of the fluid and the structural domains, a displacement compatibility criterion must be satisfied, and a traction equilibrium must be achieved at the fluid-structure interface $\Gamma_{F,S}$ shown in FIG 5. The criteria and the equilibrium equations are expressed in Equations 8 and 9, respectively.

$$d_{s,\Gamma_{F,S}} = d_{f,\Gamma_{F,S}} \tag{8}$$

$$\overrightarrow{tr_{s,\Gamma_{F,S}}} = \overrightarrow{tr_{F,\Gamma_{F,S}}} \tag{9}$$

In Equation 7, $d_{s,\Gamma_{F,S}}$ and $d_{f,\Gamma_{F,S}}$ are the displacement of the solid and the fluid at the interface, respectively. Moreover, in Equation 8, $\overrightarrow{tr_{s,\Gamma_{F,S}}}$ is the forces exerted by the solid on the interface. Similarly, $\overrightarrow{tr_{F,\Gamma_{F,S}}}$ is the force applied by the fluid on the interface.

2.5. Material selection and properties

With the governing equations completely defined, the material selection process remains for their implementation in the presented two-way coupled FSI numerical setup. In regard to the fluid domain, and as mentioned in the previous subsection, an incompressible and Newtonian with a density equal to $\rho_{\psi_f} = 1050\ kg/m^3$ and a constant dynamic viscosity of to $\mu_{\psi_f} = 0.003675\ kg/ms$. Meanwhile, for the solid domain, the mechanical properties of the artery wall material are assumed to be linear, elastic, incompressible, isotropic, and homogeneous in nature. The artery wall's Young's modulus is set at $E = 0.9\ MPa$, its density is equal to $\rho_{\psi_S} = 1120\ kg/m^3$, and a Poisson's ratio of $\nu_p = 0.45$ [69]. As for the plaque buildup, its true composition and its accompanying material properties were neglected, and thus their influence on blood flow was not considered in the numerical study. Instead, the plaque model was assumed to act as a rigid body with a no-slip surface.

2.6. Boundary conditions

The boundary conditions in a typical FSI setup, such as the presented setup, have its boundary conditions divided into two primary sections, namely the fluid domain and the solid domain, to comply to their respective governing equations.

In the fluid domain, the inlet is defined at the common carotid artery and is assumed a pulsatile Womersley profile [70]. The reason behind this boundary representation is due to its strong ability to predict the fully developed nature of the blood flow in the post-aortic section of the carotid artery [42,46]. Its implementation comes from a Navier-Stokes equation solution derivation that assumes a fully developed flow in a long, cylindrical pipe of radius R, with a rigid wall where the no-slip

condition is applied, experiencing a periodic pressure fluctuation. Moreover, the flow is assumed to be laminar, axisymmetric, and parallel to the pipe's axis. In addition, its

boundary conditions are assumed to be axisymmetric down the center. This is modelled by a momentum conservation equation defined with cylindrical coordinates as follows:

$$\frac{\partial u}{\partial t} = -\frac{1}{\rho}\frac{\partial P}{\partial x} + \nu\left(\frac{\partial^2 u}{\partial r^2} + \frac{1}{r}\frac{\partial u}{\partial r}\right) \tag{10}$$

Where ν is the kinematic viscosity. Moreover, by assuming a no-slip condition at the cylinder wall where $u = 0$ at r = R, a fluctuating pressure gradient is considered as:

$$-\frac{1}{\rho}\frac{\partial P}{\partial x} = A\cos(\omega t) = Ae^{i\omega t} \tag{11}$$

Oscillating at a frequency equal to:

$$f = \frac{\omega}{2\pi} \tag{12}$$

Where A is some constant and ω is the angular frequency. Now, by introducing Equation 11 to Equation 10, the new equation of motion then becomes:

$$\frac{\partial u}{\partial t} - \mu\left(\frac{\partial^2 u}{\partial r^2} + \frac{1}{r}\frac{\partial u}{\partial r}\right) = Ae^{i\omega t} \tag{13}$$

A further transformation of Equation 13 takes place by assuming the radius and time-dependent velocity function $u(r,t)$ to only vary with radius, such that $u(r,t) = w(r)\,e^{i\omega t}$. In turn Equation 12 becomes:

$$-\frac{i\omega}{\nu}w + \ddot{w} + \frac{1}{r}\dot{w} = -\frac{A}{\nu} \tag{14}$$

Where $\nu = {}^{\mu}\!/_{\rho}$. Lastly, by solving the given ordinary differential equation stated in Equation 14, the following general solution is obtained:

$$w(r) = -i\frac{A}{\omega}\left[1 - \frac{J_0\left(r\sqrt{\frac{-i\omega}{\nu}}\right)}{J_0\left(R\sqrt{\frac{-i\omega}{\nu}}\right)}\right] \tag{15}$$

Therefore, to define the Womersley velocity profile, $u(r,t)$, at a given pressure gradient, the solution then becomes:

$$u(r,t) = -i\frac{A}{\omega}\left[1 - \frac{J_0\left(\alpha i^{3/2}\frac{r}{R}\right)}{J_0\left(\alpha i^{3/2}\right)}\right]e^{i\omega t} \tag{16}$$

In which J_0 expresses the first kind, zero order Bessel function and α represents the Womersley number equal to $\alpha = R\sqrt{\frac{\omega}{v}}$.

To translate this mathematical expression into the Computational Fluid Dynamics (CFD) numerical setup, a User-Defined Function (UDF) is written in C language to define the pulsatile inlet velocity profile at the CCA. As for the outlet boundary, it is interpreted as a pressure boundary condition set at a gauge pressure of 0 Pa and an operating pressure of 1 atm at the two outlets of the ICA and the ECA.

The FSI interface from the fluid domain's side is defined as the inner artery wall that experiences deformations with respect to the pressure forces applied against it. Numerically, this is interpreted as deformations in the mesh, that is later introduced in Sec II E, and thus a joint-method dynamic meshing technique comprised of spring-based smoothing, dynamic layering, and local remeshing is adopted for this setup. The spring-based smoothing's working principle is simply summarized as representation of node edges as a series of interconnected springs. Moreover, the transmission of force, induced by a displacement at a neighboring boundary node, is calculated using Hooke's law[71] as follows:

$$F_i = \sum_{j}^{n_i} k_{ij}\left(\Delta x_j - \Delta x_i\right) \tag{17}$$

Where F_i is the net force, n_i is the number of neighboring nodes to node i, k_{ij} is the spring constant of the springs at the shared edge between nodes i and j. Furthermore, under the assumption of a force equilibrium at a given studied node, an iterative calculation is conducted using the Jacobi iterative method on Equation 18 until the solution converges and the final nodal position is obtained in Equation 19.

$$\Delta x_j^{n+1} = \frac{\sum_{j}^{n_i} k_{ij}\Delta x_j^{n}}{\sum_{j}^{n_i} k_{ij}} \tag{18}$$

$$x_i^{n+1} = x_i^n + \Delta x_i^{n,converged} \tag{19}$$

In Equations 17 and 18, the superscripts n and n+1 refer to the nodal positions at the current and the next time step, respectively. As for the dynamic layering method, it is a tool that operates on the basis of adding or removing layers of mesh cells positioned adjacent to the deforming interface. More specifically, the mesh cell layer undergoes splitting to create a new layer of small cells and accommodate for large deformations the carotid artery is predicted to experience during a typical pulse. Primarily, this method aids in retaining calculation stability and convergence throughout any deformational instances. Moreover, another method that supports such stability is the smoothing remeshing method. The method adopts a criterion that classifies the aspect ratio and skewness of mesh cells to evaluate their quality.

On the other hand, the structural domain boundary conditions are setup in a much simpler manner, as its numerical structural requirements are essentially locating and defining the supports of the structure and labelling the interface from the structural solver's perspective. For the current setup, a set of fixed supports are extended to the artery inlet and outlets; they are assumed at each of the inlet at the CCA and the outlets at the ICA and the ECA. This is to constraint the solid body and allow the artery to freely move in 6 degrees of freedom (DOF). Moreover, maximum displacements are expected to occur normal to the blood flow direction. As for the structural side of the interface, it has been defined at the inner wall of the cylindrical artery geometry where it coincides with the interface location specified at the fluid domain.

2.7. Discretization schemes

The presented system of governing equations in Sec II B are solved through a two-way coupled CFD-Structural solver and discretized by utilizing the finite volume method and the finite element method, respectively. For the CFD solver, a pressure-based solver was implemented for the incompressible flow problem, and a SIMPLE scheme is implemented for the pressure-velocity coupling. The reason behind this choice is because the numerical convergence of the simulation is simply because the modelled problem is assumed laminar and thus, the flow problem's convergence is constrained by the pressure-velocity coupling. Therefore, the SIMPLE scheme was chosen for a faster convergence. Moreover, given that the problem scrutinizes the FSI between the flow and the artery wall, the SIMPLE algorithm is used to address any potential instabilities due to high mesh skewness during mesh deformation [72]. As for the spatial discretization schemes, a second-order upwind scheme is used for the pressure and the momentum equations. To account for the transient nature of pulsatile flow, a transient formulation, discretized using a first-order implicit scheme, is configured with a timestep size of $\Delta T = 1\ ms$ and, 750 timesteps, and a maximum of 30 iterations per timestep. This configuration aims to capture the flow hemodynamics and the structural changes of the artery within two pulsatile cycles. Lastly, the convergence criteria used for the residuals of all governing equations was 10^{-6}. As for the structural solver, a series of linear-elastic-small-displacement stress equations were implemented to perform a linear analysis on the induced artery wall deformations.

2.8. Hemodynamic parameters

Upon solving the aforementioned governing equations, pressure and velocity solutions are stored at the center of each mesh cell; furthermore, a set of hemodynamic parameters can then be deduced to quantify local hemodynamics and scrutinize its underlying relationships with the artery's structural anomalies.

An essential parameter commonly investigated is the wall shear stress (WSS) that typically defines the tangential frictional force per unit area exerted by near-wall blood flow on the artery wall. WSS is expressed as follows:

$$\tau_w = \mu_{\psi_F} \frac{du_{\psi_F}}{dr} \tag{20}$$

In previous works, it has been concluded that oscillating values of WSS during an instant in which the WSS vector direction opposes the flow[73]. In other words, oscillatory behavior hints at the existence of blood recirculation zones. Generally, such scenarios are noted to occur in regions highly prone to atherosclerosis. Similarly, another hemodynamic parameter considered is the time-averaged wall shear stress (TAWSS) that represents the temporal average of the instantaneous WSS over a full pulse cycle. It is typically expressed as shown in Equation 21 below:

$$\tau_{taw} = \frac{1}{T} \int_0^T |\tau_w| \, dt \tag{21}$$

In which T refers to the duration of a full pulse cycle and t represents the flow time.

2.9. Mesh Independence Test

By employing the FSI numerical setup discussed in the previous sections, the computational fluid and solid domains are discretized using a structured hexahedral mesh. Specifically, an o-grid mesh is generated for the artery's domains, as shown in FIG 6. Moreover, FIG 7 illustrates the respective artery wall's structured mesh generated for the investigation.
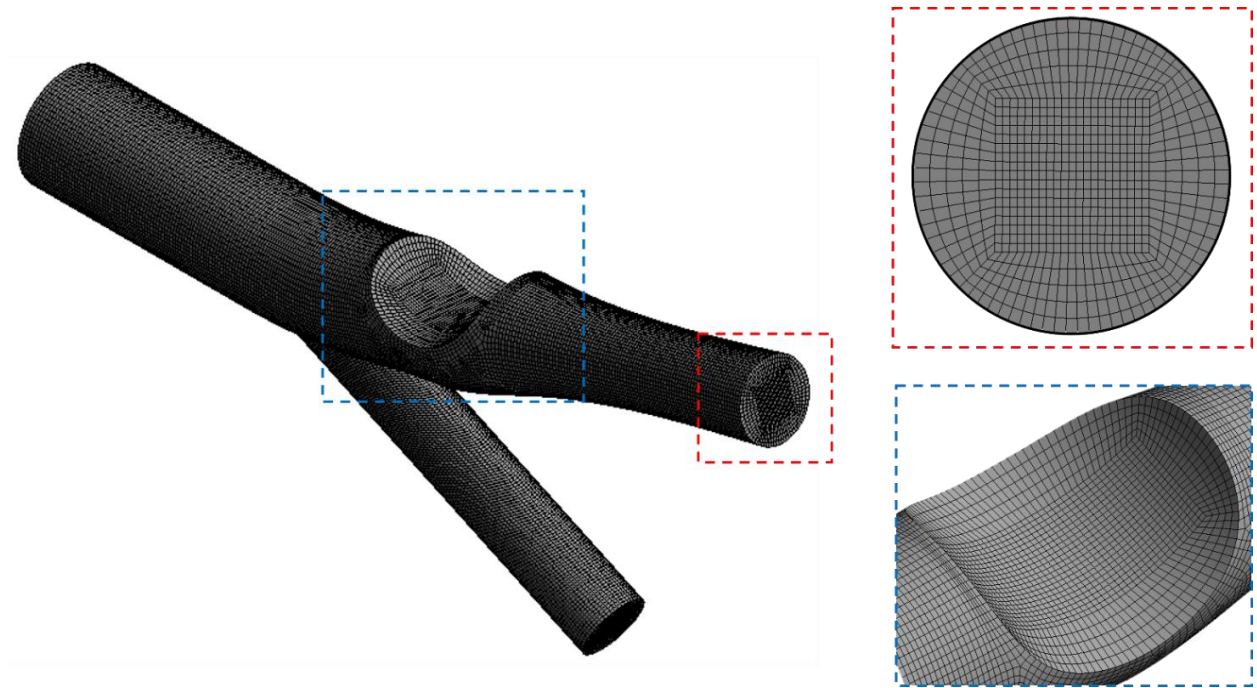
FIG. 6. Structured O-grid mesh of the fluid domain for an artery case model of 15° ICA angle and 50% ECST stenosis.
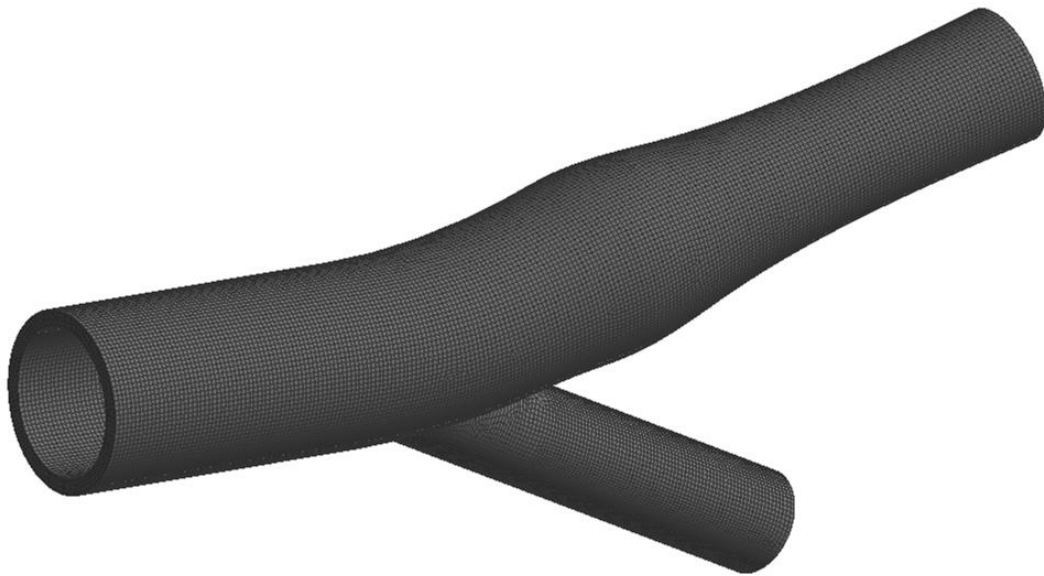
FIG. 7. Structured mesh of the solid domain for an artery case model of 15° ICA angle and 50% ECST stenosis.

A mesh independence test was performed to assess the degree of influence the mesh size had on the numerical results. Figure 8 summarizes the different mesh sizes considered for the study and their influence on the instantaneous average velocity magnitude recorded at the carotid sinus. Generally, instantaneous velocity does not witness any further significant fluctuation past the grid retaining approximately 220,000 cells. Thus, the small velocity differences past that grid are deemed negligible.
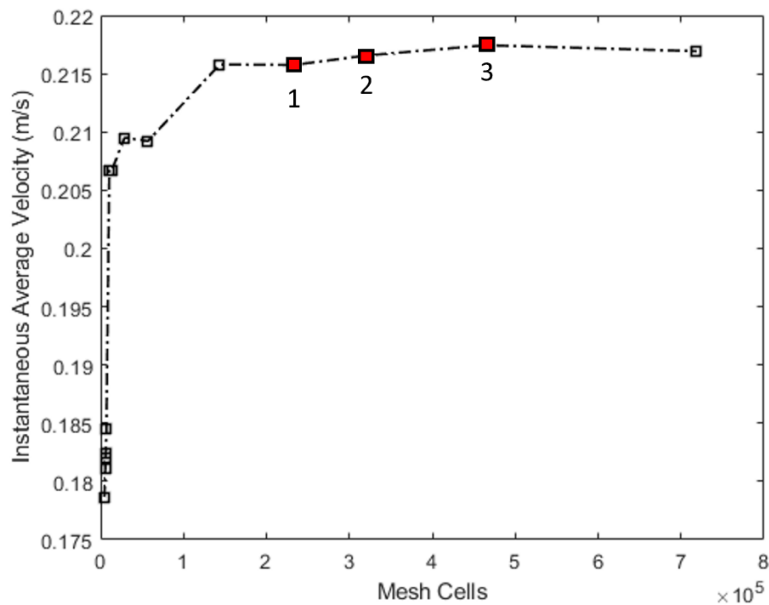
FIG. 8. Mesh independence test comparing the instantaneous average velocity obtained at Plane C recorded at flow time t = 0.75 s.

Furthermore, to scrutinize the influence of the cell size on the capturing of near-wall velocity gradients, a wall refinement sensitivity test was conducted. We have initially taken the Case 2 as our base model for conducting the analysis, where we have tested five wall refinements and collected their resultant WSS at the outer wall of Plane C. Figure 9 below draws the incremental differences between each level of near-wall mesh refinement.
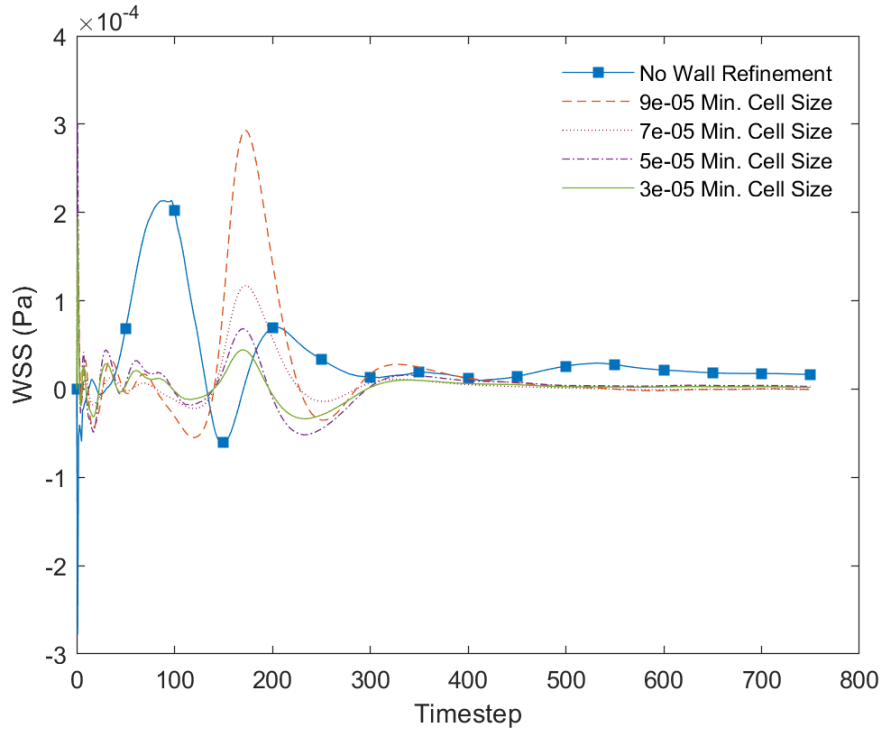
FIG. 9. Wall refinement sensitivity plot of the time evolution of the resultant WSS at Plane C outer wall with different near-wall refinements (in meters).

As illustrated, the variation in the value of WSS at the outer wall is very prominent at first, with the absence of wall refinement. However, with further refinement of the near-wall mesh, the WSS trend begins to converge with a mesh cell size of $0.05\ mm$. As such, the respective wall refinement was adopted and implemented in the artery's meshing.

2.10. Setup Validation

In addition to the mesh independence test, a setup validation is performed using the chosen grid to assess the reliability and accuracy of the suggested numerical setup and its models. Once again, the transient average velocity at Plane C is taken as a comparative parameter between the experimental and the numerical results. Here, the experimental velocity values measured in the investigation conducted by Perktold et al.[18] are used for the validation. As illustrated in FIG 10, the numerical results follow a strictly similar trend to that of the experimental values. This can be seen in the systolic phase of

the cycle. However, moving along to the diastolic phase, a noticeable divergence of numerical results from the experimental results is witnessed. Nevertheless, this discrepancy is considered insignificant, as it and thus disregarded. Moreover, such discrepancy may be resulting from ignorant assumptions in mechano-biological factors.
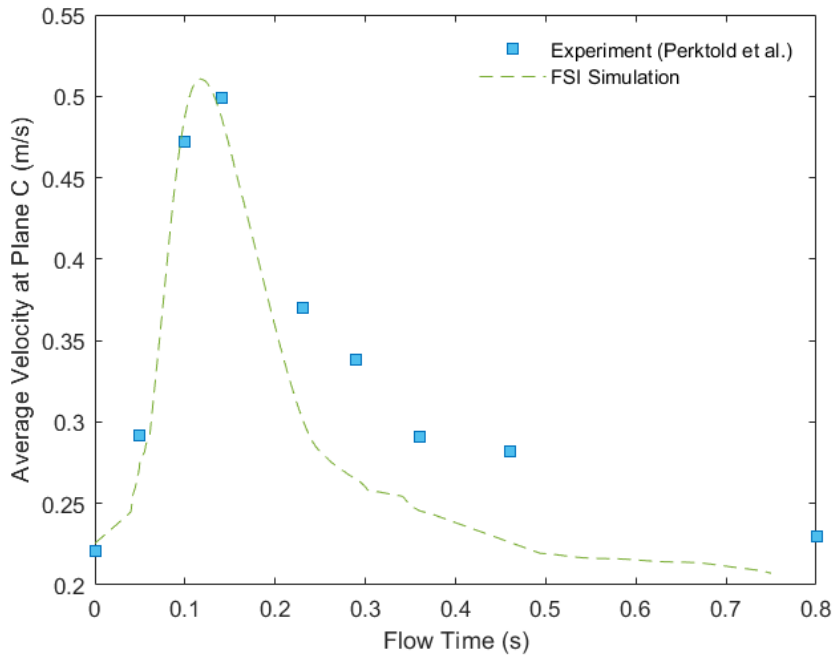
FIG. 10. A comparative plot showing difference resultant values of the average velocity at Plane C measured by Perktold et al.[18] and the presented numerical setup.

3. Results and Discussion

3.1. Developments of Blood Flow features

3.1.1.   The influence of increasing bifurcation angle on flow development

In this numerical exploration, induced blood flow structures due to varying configurations of bifurcation angles and stenosis percentages are compared. This was done through monitoring the velocity profiles and contours of the flow at different section planes along the carotid artery. Therefore, this facilitates numerical activities such as measuring the variation in blood velocity magnitude, visualizing the velocity distribution about an artery cross-section, and predicting potential vorticity formations along the artery.

By simply examining the velocity contour plots across planes A through I, multiple observations can be made on the morphing flow features as both the bifurcation angle and the degree of stenosis are gradually increased. As the bifurcation

angle widens from 15° to 40°, the velocity witnesses a slight rise in magnitude across the artery's ICA, similarly, an incremental velocity increase in the ECA at the systolic peak, as shown in FIG 11.
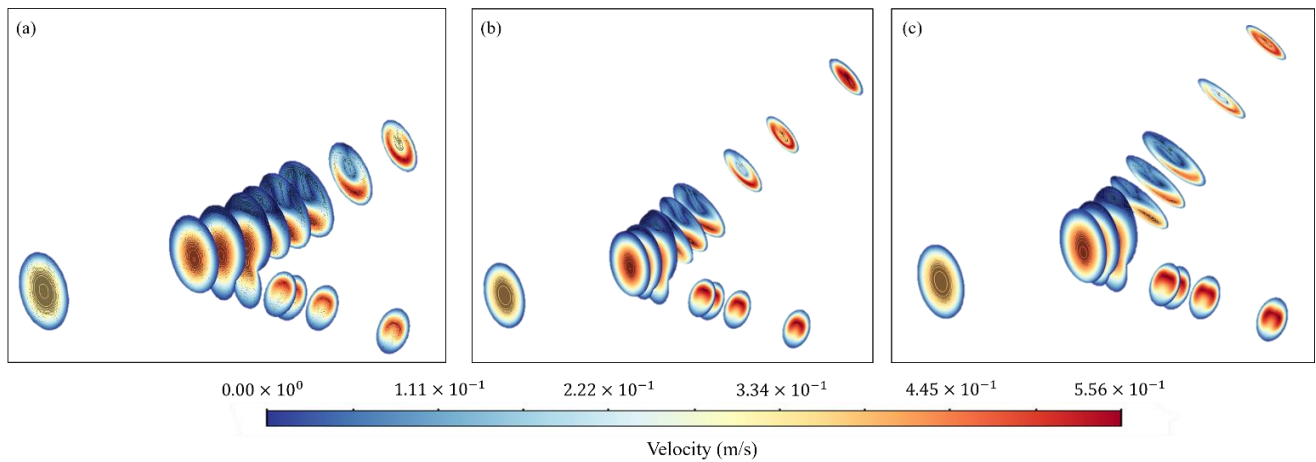
FIG. 11. Instantaneous velocity module contours plotted at Planes A to I, including the inlet and outlet planes, of a healthy artery (0% stenosis) at bifurcation angles of (a) 15° (b) 25° (c) 40° at $t = 150\Delta T$.

Figure 11 presents the instantaneous velocity at the pulse peak of the systole phase to highlight the most apparent flow feature formations. Moreover, noticeable, yet insignificant, increases in the flow recirculation at the carotid sinus are examined as the bifurcation angle gradually increased. From the series of velocity contour plots in FIG 11, it can be safely said that the velocity profiles generally retain their shape along the carotid artery, despite the small anomalies that occur due to the widening of the bifurcation angle. Nevertheless, the velocity profiles about the carotid sinus appear to experience most variation. While it still remains insignificant, it would still be of great interest to further explore the bifurcation angle's role in varying the blood flow, since bifurcation angle is clinically considered highly variable among patients. In fact, some studies have uncovered that this interpersonal variation can occur with aging and early atherosclerosis developments[74,75]. Therefore, velocity contours are plotted at Planes B through D to highlight the variation in the velocity profiles with changes to the bifurcation angle, as shown in FIG 12.
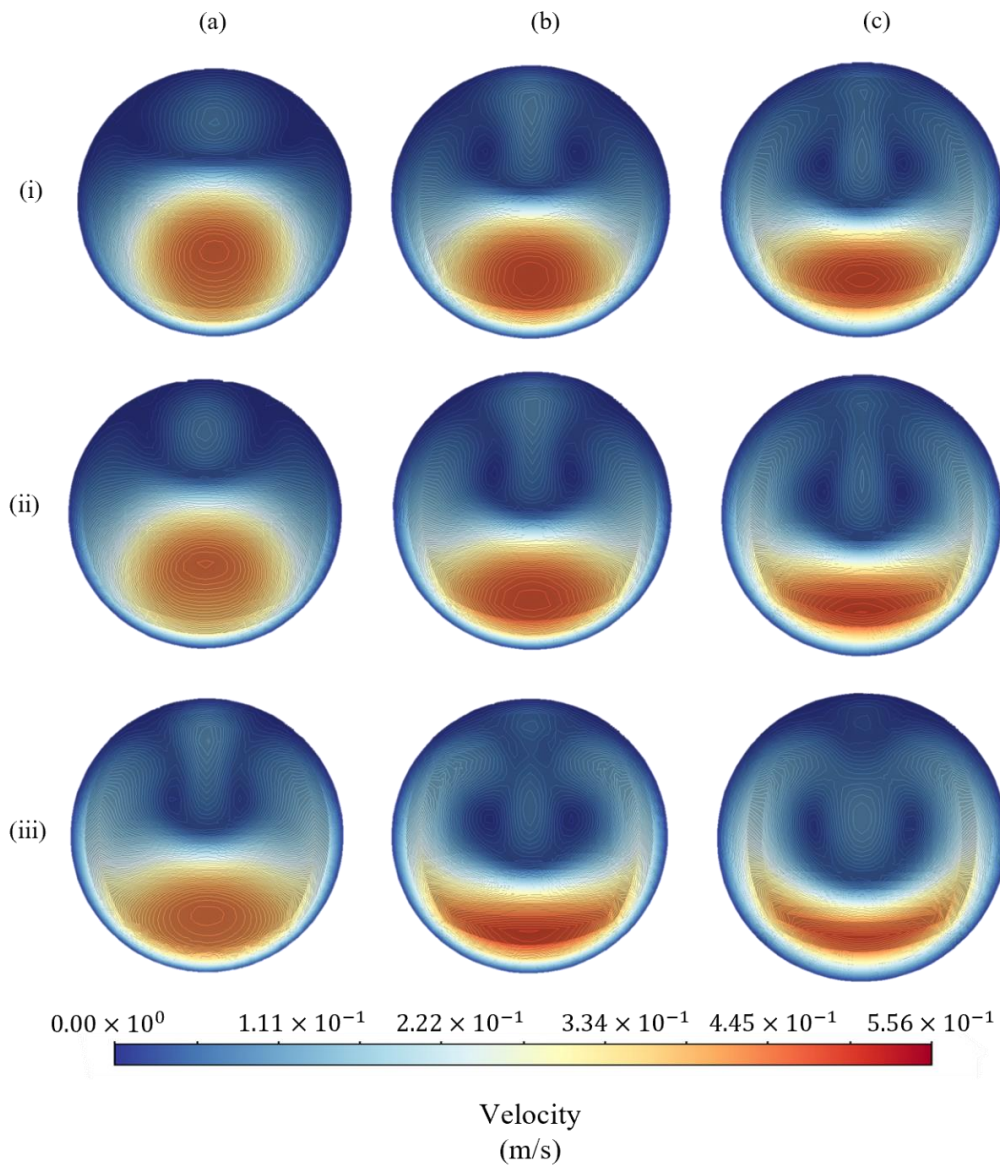
FIG. 12. Instantaneous velocity module contours plotted at (a) Plane B (b) Plane C and (c) Plane D of a healthy artery (0% stenosis) at ICA angles of (i) 15° (ii) 25° (iii) 40° at $t = 150\Delta T$.

With FIG 12 illustrating the morphing of the velocity profiles, the influence of the bifurcation angle becomes more prominent. The axial flow downstream of the ICA appears to experience gradual suppression, as jet flow is seen to develop at the ICA near wall with increasing bifurcation angle. This is justified by the traces of an expanding recirculation zone at the outer wall of the carotid sinus. From the contours, the vortex structure displaces downwards from the outer wall and thus pushing the flow against the inner wall. This is relatively more accentuated at bifurcation angles of 25° and 40°. To better visualize the recirculation zone, FIG 13 presents a set of streamline plots along the carotid artery where the recirculation zone is pronounced.

| 0.00 × 10⁰ | 5.34 × 10⁻² | 1.07 × 10⁻¹ | 1.60 × 10⁻¹ | 2.14 × 10⁻¹ | 2.67 × 10⁻¹ |
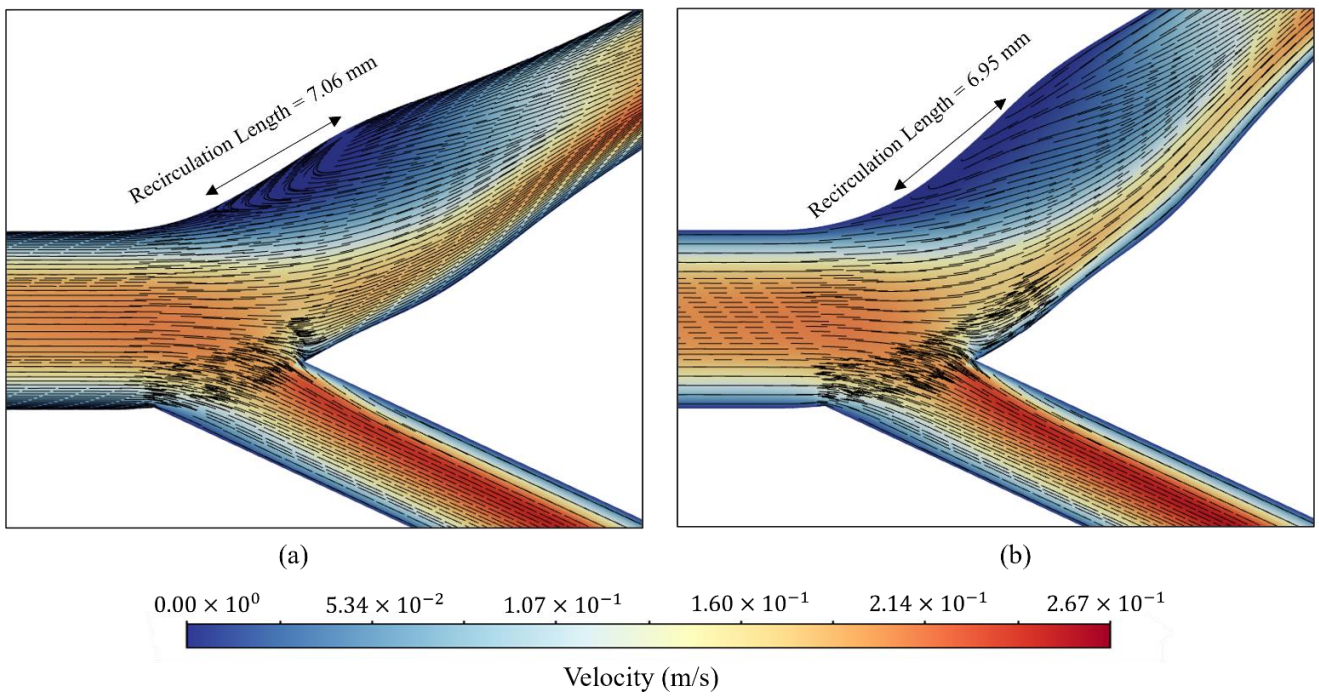
Velocity (m/s)

FIG. 13. Streamline maps plotted of a healthy artery (0% stenosis) at ICA angles of (a) 25° (b) 40° at $t = 150\Delta T$.

As FIG. 13 suggests that recirculation acts as a defining feature for the flow at the carotid sinus, monitoring the velocity gradient due to changes in the bifurcation angle becomes of great importance. Thus, FIG 14 plots the average velocity at Plane C against the flowtime. Initially, the plotted trendlines reiterate that the bifurcation angle has minimal influence on the flow; however, upon a second look, one may notice that an increase in the bifurcation angle has led to the pulse reaching a new maximum during the systolic phase. Specifically, as θ_{ICA} increases from 15° to 40°, the maximum velocity shifts from 0.467 m/s to 0.491 m/s. Moreover, this increase in θ_{ICA} has also led to a minimal shift backwards in the occurrence time of the peak. In other words, the flow would reach peak velocity at t = 0.129 s; however, with the increase of θ_{ICA}, the peak velocity is seen to occur at t = 0.123 s instead. Moving onto the diastolic phase, minimal, yet noticeable, differences in the velocity are present. Generally, it appears that at greater bifurcation angles, the velocity experiences a slight dip, but the flow follows the same trendline, nevertheless.
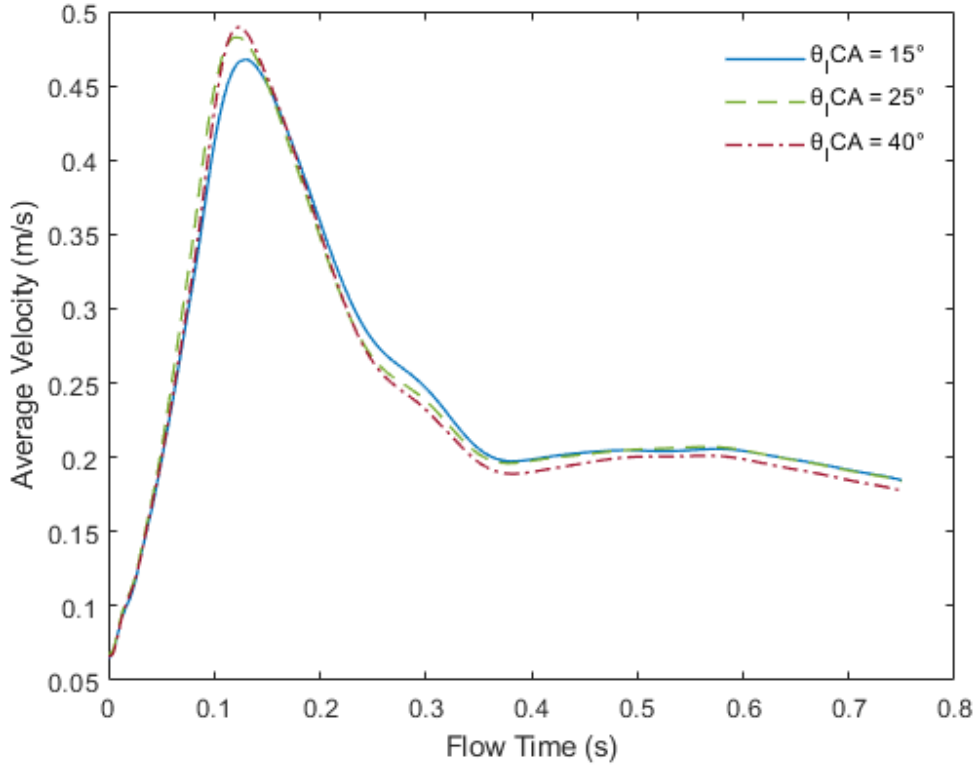
FIG. 14. Average velocity at Plane C plotted against the flow time for healthy carotid arteries (0% stenosis) at $\theta_{ICA} = 15°, 25°, 40°$.

While the FIG. 11 through 13 only present the effect of the bifurcation angle on blood flow features at 0% stenosis, it has been observed that these trends can be generalized, as they remain present at higher stenosis percentages. However, interestingly, the influence of the bifurcation angle on the flow diminishes with higher degrees of stenosis. In other words, at 50% stenosis, flow feature developments mirror the developments occurring at 0% stenosis; however, recirculation becomes more pronounced at a bifurcation angle of 40°. Meanwhile, at 70% stenosis, the recirculation zone is no longer seen expanding; however, the decrease in the velocity magnitude is still observable. Lastly, at 80% stenosis, all bifurcation angle flow effects are no longer dominant and are deemed completely negligible. This may be a step forward into truly defining the causation of the clinical correlation between large bifurcation angles, typically assumed to be $\theta_{ICA} > 25°$, and early developments of atherosclerosis. However, to safely reach conclusive remarks on it, reliable hemodynamic parameters, such as the wall shear stress (WSS), must be monitored, as shown later in Sec. III B.

3.1.2. The influence of increasing stenosis percentage on flow development

On the other hand, another geometrical variation induced by atherosclerosis developments is the dilating lump-shaped plaque accumulation, otherwise known as stenosis. Following a similar qualitative procedure, a series of vector plots are

collected to qualitatively analyze the flow manipulations stenosis induces in the ICA. It has been noted that with the gradual increase of stenosis, prominent flow features, such as the main recirculation zone at 0% stenosis, morph and develop into new features. Intriguingly, an increase of stenosis from 0% to 50% does not appear to influence the main flow significantly. In fact, the velocity profiles throughout the ICA and ECA at 50% stenosis mirrors those captured at 0% stenosis, as shown in FIG 15.
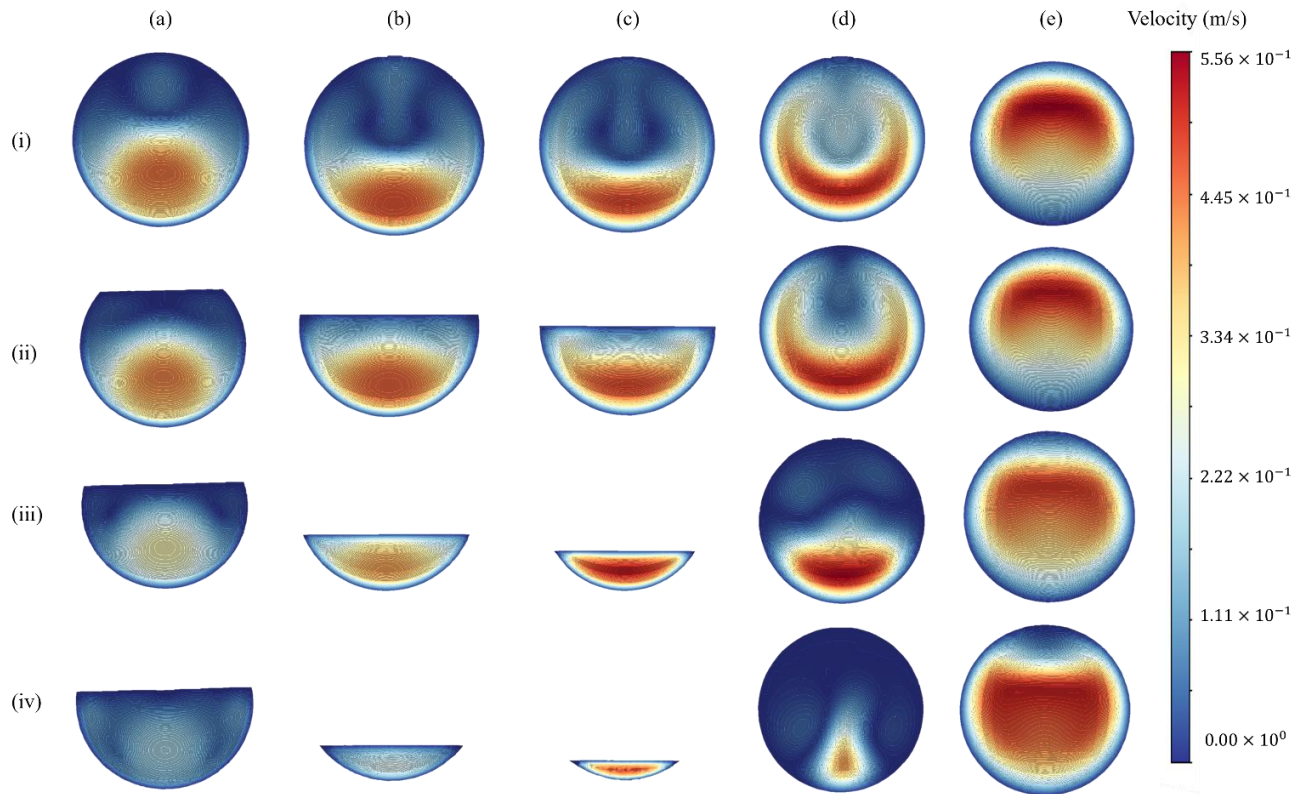
FIG. 15. Instantaneous velocity module contours plotted at (a) Plane B (b) Plane C (c) Plane D (d) Plane E (e) Plane G of arteries with $\theta_{ICA} = 25°$ experiencing different degrees of stenosis (i) 0% (ii) 50% (iii) 70% (iv) 80% at $t = 150\Delta T$.

However, with the increase of stenosis to 70%, the clogging becomes more significant in its manipulation of flow. By simply looking at the velocity contour plots, it can be easily noticed that the flow has reduced at the ICA, specifically about the carotid sinus. Moving downstream the sinus, a critical case of jet flow forms at the converging cross-sectional area of the sinus. Moreover, at Plane E, the flow at the ICA past the sinus also appears to have been affected, as traces of formations of two vortices at the outer wall is observed. However, upon examining the velocity contour plot at Plane G, yet another flow change is noticed at the ECA. The flow about the outer wall of the ECA appears to be plunging towards the axis of the artery section. Similarly, as the stenosis is further increased to a maximum of 80%, the new flow formations witnessed at 70%

stenosis simply increase in intensity to a point where the formed vortices downstream of the ICA experience a shift in position from the outer wall towards the sidewalls of the ICA. This, in return, forces the jet flow towards the center against the inner wall. Meanwhile, the flow at the ECA further plunges from the outer wall. While the contour plots have uncovered these interesting flow trends, streamline plots would further enhance the visualization of the aforementioned flow manipulations, as demonstrated in FIG 16.
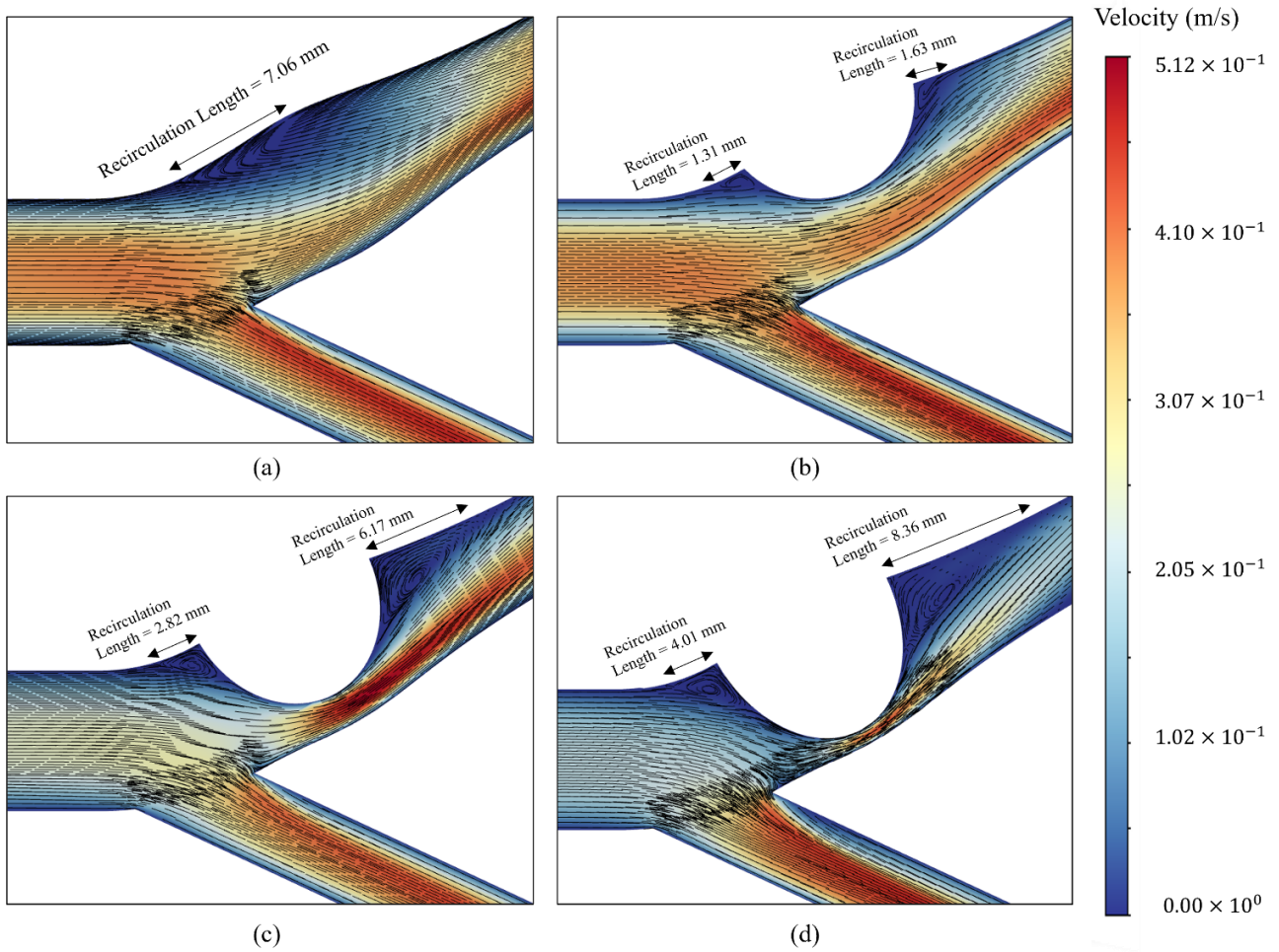
FIG. 16. Streamline maps plotted for arteries with $\theta_{ICA} = 25°$ experiencing different degrees of stenosis (a) 0% (b) 50% (c) 70% (d) 80% at $t = 150\Delta T$.

As shown in FIG 16, the singular recirculation zone drawn in FIG 16a is split into two regions by the stenosis occurring at the maximum diameter of the carotid sinus. Moreover, the observation of increased recirculation intensity with the increase of the stenosis is reiterated in the streamline figures, and thus, one may see the hemodynamic significance stenosis has on blood flow.

As opposed to the minimalistic flow effect induced by the change in the bifurcation angle, increasing stenosis does in fact drastically vary the flow velocity and its profiles, as presented earlier in FIG 15. With new formations of vortices about the stenosed sinus, the flow characteristics about the sinus region becomes of great interest. Figure 17 plots the average recorded velocity at Plane C at different cases of artery stenosis with respect to flow time. As expected, with the creation of a converging area and with the flow constrained, a jet flow is induced, consequently. This then justifies the drastic hike in velocity magnitude with the increase of the percentage of stenosis. The trend begins with the increase in stenosis from 0% to 50% with a relatively insignificant change in terms of velocity magnitude. However, the initial rate at which velocity reaches its peak witnesses a noticeable increase. This trend is inherited and intensified with the advancement of stenosis. As a matter of fact, a new flow behavior begins to emerge at 70% stenosis, where the velocity experiences slight instability during the diastolic phase between $t = 0.2 - 0.4$ s. The increasing velocity gradient and the instability can possibly be justified by the instable behavior of the vortices upstream and downstream of the stenosed region, respectively.
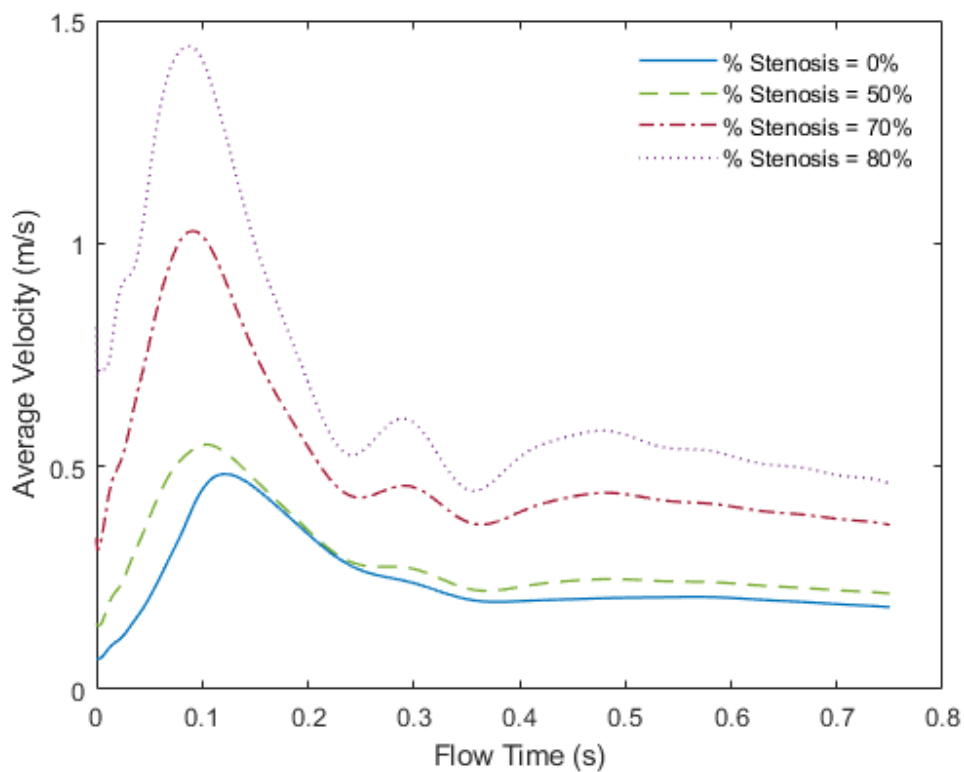
FIG. 17. Average velocity at Plane C plotted against the flow time for carotid arteries at $\theta_{ICA} = 25°$ experiencing stenosis percentages of $0\%, 50\%, 70\%, 80\%$.

To reiterate, such recirculation embodies a flow constraint on the blood which reduces the blood and causes abnormalities in the pulse cycles. However, to truly define the role of vortices and their physiological impacts on the artery as a whole, the wall shear stress and wall displacements must be quantified and scrutinized, as shown in later sections.

3.2. Variations of the Wall Shear Stress with Changes in the Arterial Geometrical Features

The wall shear stress has been recognized as a prominent clinical hemodynamic parameter that characterizes the developments of atherosclerosis. Moreover, it aids in uncovering underlying progression and regression mechanisms of atherosclerotic stenosis. Therefore, in this section, the WSS is quantified with flow time at geometrical instances of varying ICA angles and degrees of stenosis. As blood flow has been seen witnessing the most variation, with respect to the geometrical manipulations in the bifurcation angle and degree of stenosis, at the carotid sinus, the WSS was monitored by recording its values at the outer and inner sinus walls at each of Planes C and D.
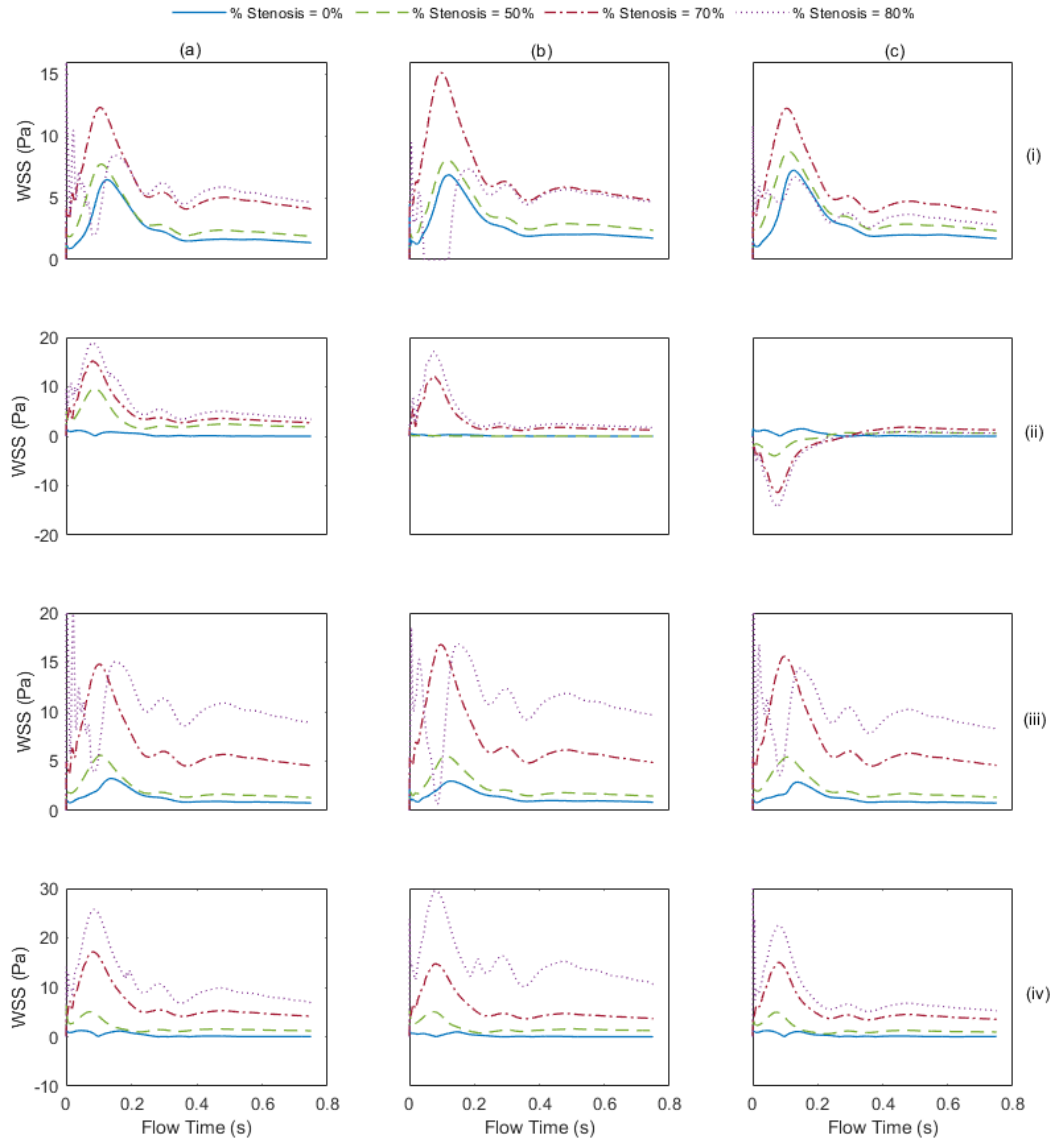
FIG. 18. Recorded WSS values in the axial direction at Planes C and D plotted against flow time at (a) $\theta_{ICA} = 15°$ (b) $\theta_{ICA} = 25°$ (c) $\theta_{ICA} = 40°$ at monitor points placed about (i) Plane C inner wall (ii) Plane C outer wall (iii) Plane D inner wall (iv) Plane D outer wall.

Figure 18 presents the change in WSS at cases where $\theta_{ICA} = 15°, 25°, 40°$ and percentage stenosis of 0%, 50%, 70%, and 80%. Essentially, the plots reveal an interesting contrast between WSS' behavior towards the changing geometrical configurations at the inner wall and the outer wall. At the inner wall of Plane C, a gradual hike in WSS magnitude can be observed, as stenosis rises from 0% to 70%. However, as stenosis is increased to 80%, a general drop in WSS magnitude is witnessed, with a severe drop during the systolic peak. A similar trend is observed at the inner wall of Plane D, however, WSS generally sustains an increasing magnitude from 0% to 70% stenosis, after the sharp drop at the systolic peak. As for the outer walls, interestingly, WSS, in terms of magnitude, is seen to exhibit a different trend, specifically, at the systolic peak. Instead, WSS retains a continuous rise at the systolic peak with the increase of stenosis from 0% through to 80%.

Furthermore, upon examining the effect of stenosis on WSS, the similarity of WSS values at 0% and 50% stenosis becomes quite noticeable. In fact, at the inner wall of Plane C, the gradient between the values is minimal. However, a prominent difference that is highlighted is that an increase in stenosis to 50% leads to an increase in the rate at which WSS rises about the systolic peak. On the other hand, and as aforementioned, this observation dissolves upon increasing stenosis to 70%. Instead, another eye-catching trend emerges where WSS begins to experience oscillations towards the diastolic phase. This can be seen at t = 0.2 − 0.4 s, which expectedly overlaps with the velocity fluctuation witnessed in FIG 17. This reiterates the relationship between WSS and the flow velocity at near-wall regions. Typically, these fluctuations may hint at the formation of recirculatory flows. As a matter of fact, clear evidence of recirculation is primarily shown at the outer walls of Plane D, which are specifically highlighted by the negative WSS values. For example, the healthy artery models consistently demonstrate negative WSS values regardless of the bifurcation angle. However, the role of the bifurcation angle is highlighted by the negative WSS values obtained at Plane C's outer wall for all cases of stenosis. This is because these oscillations appear to be more amplified at the outer walls with the increase of ICA angle to 40°, where it has been revealed that violent vortices are formed, as shown in FIG 15.

Figure 19 enables a closer examination of the true effects of bifurcation angle variation on the WSS by plotting the WSS magnitude. The carotid artery stenosis cases considered in the figure are 50% and 70% stenosis, as it highlights the transition stage to severe stenosis according to the ECST criterion. Interestingly, the bifurcation angle effect is presented differently at each case of stenosis. For instance, at 50% stenosis, WSS appears noticeably higher at $\theta_{ICA} = 15°$ in most cases, with the exception of the inner wall at Plane C. Meanwhile, at 70% stenosis, the trend in which WSS is maximum at $\theta_{ICA} = 15°$ remains at the outer wall of Planes C and D; however, it diminishes at the planes' inner walls. Instead, WSS is shown to reach a maximum at an ICA angle of $\theta_{ICA} = 25°$.
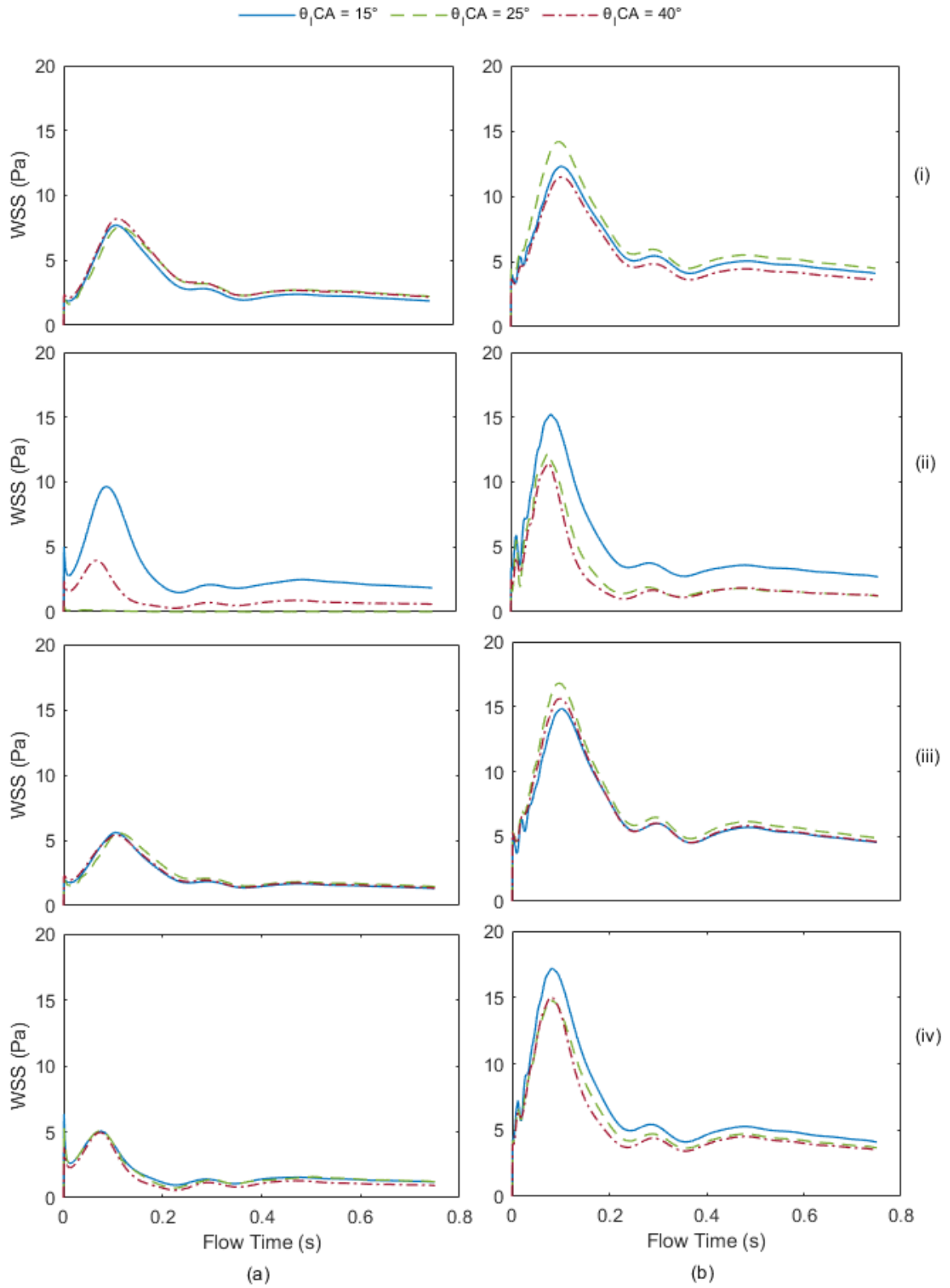
FIG. 19. WSS magnitude varying with ICA angles at Planes C and D plotted against flow time at (a) 50% Stenosis (b) 70% stenosis at monitor points placed about (i) Plane C inner wall (ii) Plane C outer wall (iii) Plane D inner wall (iv) Plane D outer wall.

The observed changes in WSS values with respect to both bifurcation angle and the percentage stenosis has shown an interesting contrast mainly between the inner and the outer walls at different geometries of the artery. When comparing the influence of stenosis, it seems that the more severe the degree of stenosis was, the higher the WSS became. With WSS clinically known as an indicator of potential atherosclerosis development[76], one might interpret the low WSS magnitude attained at healthy and mild stenosis (0% and 50%) as a higher probability of plaque build-up compared to severe cases of advanced atherosclerosis plaque (70%, 80%). Typically, the mechanism of plaque formation initiation at locations that sustain low WSS levels is explained as an increase in endothelial cell permeability, which in turn, induces increased lipoprotein retention, as explained by Moerman et al.[77]. Moreover, regulation of pro-inflammatory signaling pathways then leads to increased concentrations of inflammatory cells. Therefore, with reference to the numerical models, plaque is more prone to form throughout the outer walls of the carotid sinus (Planes C and D) of healthy models. In addition, stenosed models (50%-80%) show potential of further plaque development upstream of the existing plaque at the outer walls of the sinus, specifically in cases of a 40° ICA angle. On the other hand, the higher WSS values at the severe cases are interpreted as a higher probability of plaque rupture[78]. Such values are observed mainly at the outer wall of the sinus at Planes C and D. Moreover, this trend is sustained across all degrees of stenosis. The reason behind this attribution is because many studies have consistently observed high WSS at the plaque rupture site. However, Eshtehardi et al.[79] suggests high WSS inducing high intra-plaque stress as a potential mechanism for plaque rupture. Perhaps, this may be one of the major reasons as to why the ECST criterion considers cases of stenosis > 70% surgery-required cases. This is because plaque rupture is the main mechanism of thrombosis[80] where the rupture exposes cholesterol and tissue under the fibrous cap, initiates the formation of a blood clot at rupture site, and the growing clot eventually blocks the blood flow in the artery. However, another trend witnessed with increase of stenosis is the sharp drop in WSS at the inner walls upon reaching the systolic peak. Similarly, this might hint at an instant at which plaque buildup is encouraged at the inner walls, where the once eccentric stenosis develops into a concentric stenosis. This is probably due to the flow disturbances, i.e. vortex formations, that lead to endothelial inflammation[81,82].

Moreover, looking at the effect of the bifurcation angle, the aforementioned effects are amplified differently based on the stenosis experienced. As it seems at 50%, the drop in WSS is generally not significant at the inner walls of Planes C and D and the outer wall of Plane D. However, it is noticeable at the outer wall of Plane C, which, as interpreted earlier, suggests that the plaque buildup is induced with the increase of the ICA angle. As for 70% stenosis, a relatively larger variation in the WSS is observed. At the inner walls, WSS observes opposing trends as the ICA angle is increased; WSS increases as the ICA angle increases to 25° and then decreases to a new low after a further angular increase to 40°. As for the outer walls, they

generally experience a more pronounced effect of what was witnessed at 50% stenosis, where the risk of plaque rupture decreases with the increase of the ICA angle.

3.3. Flow-Induced Geometrical Deformations of the Carotid Artery

With hemodynamic flow features defined through monitoring changes in the direction of flow, flow velocity and WSS at the artery walls, it would be insightful to identify the effects this variation of flow has on the reciprocating structural deformations experienced by the artery wall at each of the considered cases. Figure 20 quantifies and summarizes the change in the total deformation witnessed at the artery wall at each combination of degree of stenosis and bifurcation angle. It has been revealed that the bifurcation angle and the degree of deformation share a general negative relationship. With the increase of the ICA angle, an interesting trend was captured in which the deformation was initially inhibited, as θ_{ICA} was increased from 15° to 25°, but witnessed incremental amplification after further increasing the angle to 40°. This trend remains very consistent at 0%, 50%, and 70% stenosis. However, at 80% stenosis, the trend witnesses a slight shift in order. An increase in the ICA angle from 15° to 25° leads to a surprising increase in the total arterial deformation. Moreover, with a further increase to 40°, the deformation is instead inhibited significantly. This appears to violate the observation made by Batwal et al.[83] where deformation witnessed a relative drop in the stenosed artery. Perhaps, it is because of the lack of emphasis placed on the role of the bifurcation angle in the wall deformation. In addition, it has been revealed that the ICA angle retains, to a certain extent, an effect on the time at which maximum deformation occurs. This is mainly noticeable at cases of 0% stenosis shown in FIG 20a where the maximum deformation for ICA angles of 15° occurs at t = 0.077 s. Meanwhile, cases with an ICA angle of 25° witness their maximum deformation at t = 0.07 s, while a maximum deformation occurs at t = 0.105 s, at 40°. However, this effect wears out as soon as stenosis is increased past 0%. This trend is summarized in Table 3.
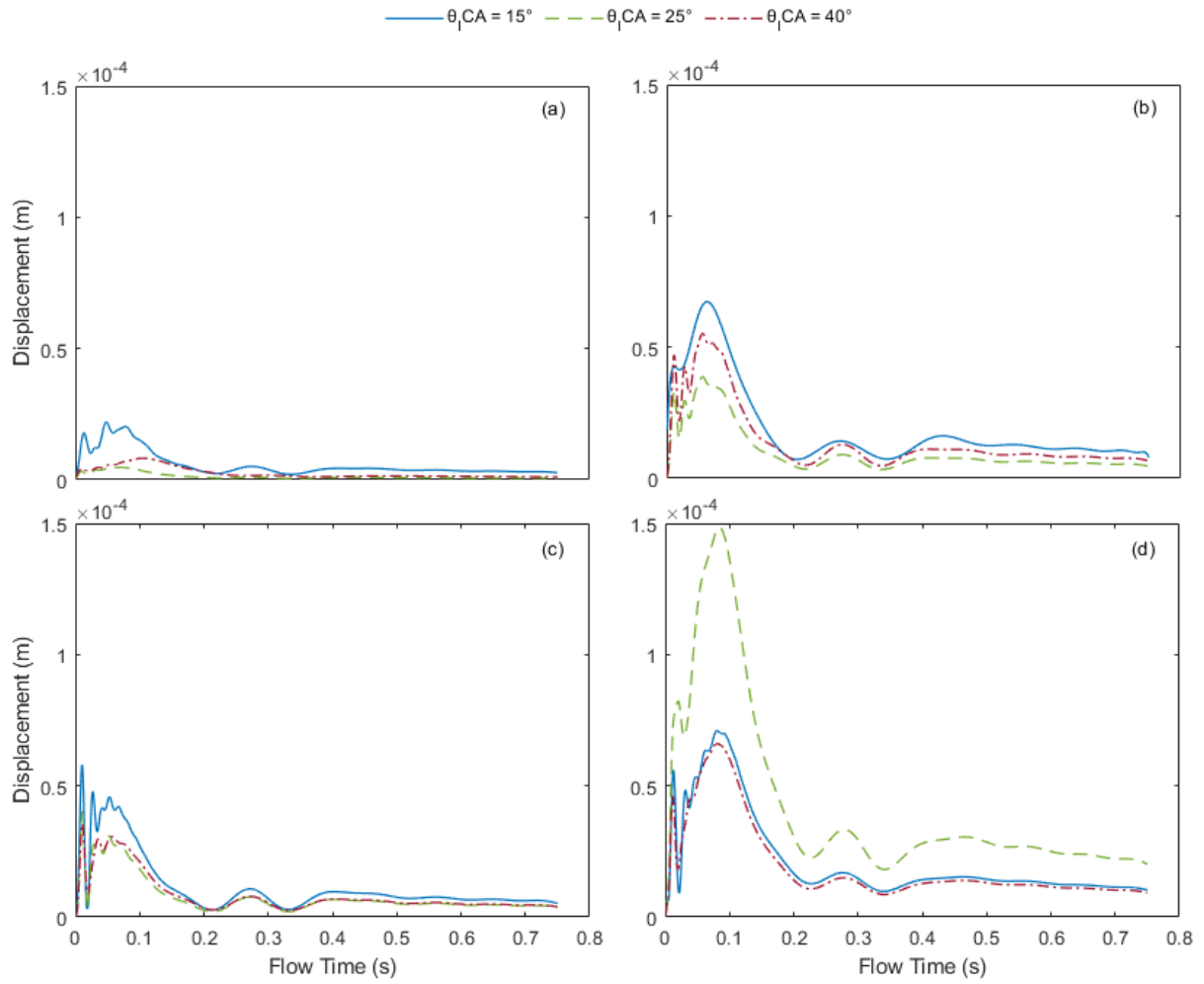
FIG. 20. Maximum total wall displacement of artery wall plotted against flow time for stenosis cases of (a) 0% (b) 50% (c) 70% (d) 80%.

However, when upon examining the influence of stenosis on the total deformation, a negative trend is revealed at the presence of stenosis as it is increased to 50%. And thus, the instant at which maximum deformation is pushed further back before the systolic peak. However, as stenosis progresses further, this time instant slowly climbs back towards the systolic peak instant. On the other hand, deformation-wise, it follows a similar alternating trend where total deformation drastically rises with the progression of stenosis to 50%. However, a relatively slight drop is witnessed at 70%, which is later rectified and increased at 80%. In addition to that, stenosis progression consistently induces frequent oscillations of arterial deformation during the late diastolic phase regardless of the ICA angle, however, only during the presence of stenosis.

Table 3. Flowtime at which maximum deformation occurs for each combination of cases.

ECST Percentage of Stenosis	ICA Angle, $\theta_{ICA}(°)$		
	15	25	40
0%	0.077 s	0.070 s	0.105 s
50%	0.055 s	0.054 s	0.064 s
70%	0.054 s	0.051 s	0.057 s
80%	0.082 s	0.086 s	0.085 s

Typically, the majority of deformations about a carotid artery would occur at the sides of the apex, just before the carotid sinus. This observation has been consistent throughout the literature[83,84], despite introducing both eccentric and concentric stenosis. Similarly, this incident has been observed in the cases of 0% to 70% stenosis. However, as 80% presents an anomaly in the deformation trend, the condition also demonstrates an unexpected change in points of deformation. While the general region of deformation about the carotid sinus and apex remains unchanged, as illustrated in FIG 21, the patch of maximum deformation jumps from one side to another with the variation of the ICA angle. At 15°, the deformation still occurs at the sidewalls of the apex with some minor deformations about the outer wall of the carotid sinus. As the ICA angle becomes 25°, deformation at the apex sidewalls is noticeably inhibited, however, maximum deformation is witnessed at the outer wall within the region of the apex. Lastly, at 40°, surprisingly, the deformation at the apex sidewalls returns alongside a new region of maximum deformation about the carotid sinus.
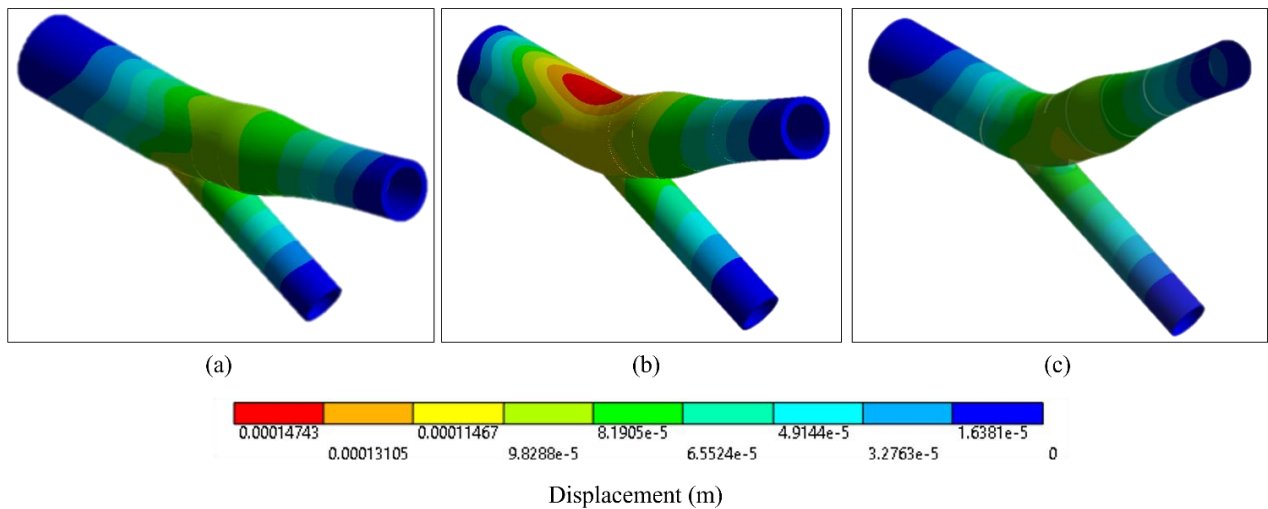
FIG. 21. Contour plots of total deformation (in meters) experienced by the artery wall of an artery experiencing 80% stenosis for ICA angles of (a) $\theta_{ICA} = 15°$ (b) $\theta_{ICA} = 25°$ (c) $\theta_{ICA} = 40°$ at their respective maximum deformation time instant.

4. Conclusion

In this numerical physiological investigation, a parametric analysis has been conducted to scrutinize the interpersonal geometrical differences of one's carotid artery by uncovering the role of two geometrical variations primarily examined in a typical carotid artery, namely the bifurcation angle and the degree of stenosis. The bifurcation angle has been varied by keeping the ECA angle constant while varying the ICA angle from 15°, 25°, and to 40°. As for the stenosis, an eccentric stenosis has been considered for the carotid artery models with varying severity from 0%, 50%, 70%, and to 80%, as per the ECST criterion. Thus, the stenosis shape was assumed cylindrical throughout this study. This model was coupled with a structural model of the artery wall to explore the influence of flow on the wall structure. Through capturing the developments of flow features within each carotid artery model, monitoring its velocity values, tracking the change in the WSS, and observing the resultant arterial deformations, multiple conclusions were made on the hemodynamic relationship between the flow and the artery structure. The following key conclusions were drawn from this investigation:

- Upon monitoring the formations of flow structures at different geometrical cases, it has been observed that an increase in the bifurcation angle slightly amplifies existing recirculation zones. Meanwhile, a progression in the stenosis seems to split the naturally occurring recirculation zone about the outer wall of the sinus into two smaller recirculation zones upstream and downstream of the carotid sinus. Moreover, flow about the ICA sidewalls is inhibited by the vortices, in addition to the formation of jet flow about the inner wall of the sinus.

- Similarly, the wall shear stress undergoes parameter-based variation where a complementary effect takes place depending on the bifurcation angle set and the degree of stenosis observed. With the increase of the bifurcation angle, given that stenosis is < 50%, the value of WSS experiences a noticeable drop in value at the ICA outer walls in a way that induces further development of existing plaque buildup. However, for stenosis ≥ 70%, WSS value begins to drop in value near the inner walls instead where concentric stenosis may be encouraged. Furthermore, WSS begins to rise at the outer walls which may lead to increased risk of plaque rupture simultaneously.

- The influence of hemodynamic flow variation on the artery structure is quantified by its total displacement. It has been generally noted that the total deformation witnessed at the artery wall decreases with the increase of the bifurcation angle. Moreover, an increase in stenosis generally presents an increase in total deformation. However, a stenosis of 80% demonstrates an exception in deformation where it experiences a significant increase upon increasing the bifurcation angle. Moreover, this exceptional behavior carries forward with the positioning of deformation where the point of maximum deformation moves from its original position at the sidewalls of the apex to the outer walls of carotid sinus.

The parametric study presents interesting complementary effects and trends that are found at different instances of bifurcation angles and stenosis severities. Thus, this only highlights the complexity of generalizing stenosis cases and emphasizes the importance of patient-specific assessment during a stenosis diagnosis. Despite that, general trends were still able to be drawn granting a better understanding of the health risks potentially posed on the patient at cases of high bifurcation angles and high stenosis severities. However, a suggested continuation of the presented work would be further scrutinizing the development of plaque buildup and its rupture to reliably assess the aforementioned health risks.

Conflict of Interest

All authors certify that they have no affiliations with or involvement in any organization or entity with any financial interest or non-financial interest in the subject matter or materials discussed in this manuscript.

AUTHORS' CONTRIBUTIONS

B.A. developed the model, performed the analysis, and wrote the manuscript. Y.H.S. conceptualized the methodology. G.S. advised the fluid dynamics methodology and provided support on its analysis. Both A.C.T.Y. and G.S. supported the manuscript's revision.

DATA AVAILABILITY

The data that support the findings of this study are available from the corresponding author upon reasonable request.

REFERENCES

[1] A. Hoffmann, P. Chockalingam, O. H. Balint, A. Dadashev, K. Dimopoulos, R. Engel, M. Schmid, M. Schwerzmann, M. A. Gatzoulis, B. Mulder, and E. Oechslin, Heart **96** (15), 1223 (2010).

[2] P. J. Barnes, S. D. Shapiro, and R. A. Pauwels, Eur Respir J **22** (4), 672 (2003).

[3] F. Sanchis-Gomar, C. Perez-Quilis, R. Leischik, and A. Lucia, Ann Transl Med **4** (13), 256 (2016).

[4] (World Health Organization, 2021).

[5] M. S. Phipps and C. A. Cronin, BMJ **368**, l6983 (2020).

[6] R. Lisak, D. Truong, W. Carrol, and B. Roongroj, *International Neurology*. (Wiley, New York, 2016).

[7] J.-H. Kim, Y.-J. Jung, and C.-H. Chang, Journal of Cerebrovascular and Endovascular Neurosurgery **19** (2) (2017).

[8] Y. Qiu, D. R. Myers, and W. A. Lam, Nat Rev Mater **4** (5), 294 (2019).

9   C. Zhang, S. Xie, S. Li, F. Pu, X. Deng, Y. Fan, and D. Li, J Biomech **45** (1), 83 (2012).

10   C. K. Zarins, D. P. Giddens, B. K. Bharadavj, V. S. Sottiurai, R. F. Mabon, and S. Glagov, Circulation Research **53** (4), 502 (1983).

11   B. K. Bharadavj, R. F. Mabon, and D. P. Giddens, Journal of Biomechanics **15** (5), 349 (1982).

12   Z. Sun and L. Xu, Comput Med Imaging Graph **38** (8), 651 (2014).

13   D. A. Steinman, Cardiovascular & Haematological Disorders **4**, 183 (2004).

14   A. Acuna, A. G. Berman, F. W. Damen, B. A. Meyers, A. R. Adelsperger, K. C. Bayer, M. C. Brindise, B. Bungart, A. M. Kiel, R. A. Morrison, J. C. Muskat, K. M. Wasilczuk, Y. Wen, J. Zhang, P. Zito, and C. J. Goergen, J Biomech Eng **140** (8), 0808011 (2018).

15   C. G. Caro, J. M. Fitz-Gerald, and R. C. Schroter, Nature **233**, 1159 (1969).

16   C. G. Caro, J. M. Fitz-Gerald, and R. C. Schroter, Proc R Soc Lond B Biol Sci **177** (1046), 109 (1971).

17   D. N. Ku, D. P. Giddens, C. K. Zarins, and S. Glagov, Arteriosclerosis **5** (3), 293 (1985).

18   K. Perktold, M. Resch, and R. O. Peter, Journal of Biomechanics **24** (6), 409 (1991).

19   G. A. Donnan, S. M. Davis, B. R. Chambers, and P. C. Gates, The Lancet **351**, 1372 (1998).

20   I. N. Staikov, M. Arnold, H. P. Mattle, L. Remonda, M. Sturzenegger, R. W. Baumgartner, and G. Schroth, Journal of Neurology **247**, 681 (2000).

21   G. A. Donnan, S. M. Davis, B. R. Chambers, and P. C. Gates, Lancet **351** (9113), 1372 (1998).

22   P. M. Rothwell, R. J. Gibson, J. Slattery, R. J. Sellar, and C. P. Warlow, Stroke **25** (12), 2435 (1994).

23   L. Saba and G. Mallarini, Eur J Radiol **76** (1), 42 (2010).

24   L. Saba, C. Loewe, T. Weikert, M. C. Williams, N. Galea, R. P. J. Budde, R. Vliegenthart, B. K. Velthuis, M. Francone, J. Bremerich, L. Natale, K. Nikolaou, J. N. Dacher, C. Peebles, F. Caobelli, A. Redheuil, M. Dewey, K. F. Kreitner, and R. Salgado, Eur Radiol (2022).

25   K. Perktold, R. O. Peter, M. Resch, and G. Langs, Journal of Biomedical Engineering **13**, 507 (1991).

26   T. Saho and H. Onishi, Radiol Phys Technol **9** (2), 277 (2016).

27   K. T. Nguyen, C. D. Clark, T. J. Chancellor, and D. V. Papavassiliou, J Biomech **41** (1), 11 (2008).

28   T. Chaichana, Z. Sun, and J. Jewkes, J Biomech **44** (10), 1869 (2011).

29   M. F. Rabbi, F. S. Laboni, and M. T. Arafat, Informatics in Medicine Unlocked **19** (2020).

30   G. Liu, J. Wu, D. N. Ghista, W. Huang, and K. K. Wong, Comput Biol Med **64**, 117 (2015).

31   M. H. Friedman, A. M. Brinkman, J. J. Qin, and W. A. Seed, Atherosclerosis **98**, 193 (1993).

[32]   C. Chiastra, D. Gallo, P. Tasso, F. Iannaccone, F. Migliavacca, J. J. Wentzel, and U. Morbiducci, J Biomech **58**, 79 (2017).

[33]   S. Beier, J. Ormiston, M. Webster, J. Cater, S. Norris, P. Medrano-Gracia, A. Young, and B. Cowan, J Biomech **49** (9), 1570 (2016).

[34]   S. W. Lee, L. Antiga, J. D. Spence, and D. A. Steinman, Stroke **39** (8), 2341 (2008).

[35]   F. J. H. Gijsen, F. N. Van De Vosse, and J. D. Janssen, Journal of Biomechanics **32**, 601 (1999).

[36]   J. Chen and X. Y. Lu, J Biomech **37** (12), 1899 (2004).

[37]   M. Dabagh, P. Vasava, and P. Jalali, Med Biol Eng Comput **53** (5), 463 (2015).

[38]   D. N. Ku, Annual Review of Fluid Mechanics **29**, 399 (1997).

[39]   M. Colombo, M. Bologna, M. Garbey, S. Berceli, Y. He, J. F. Rodriguez Matas, F. Migliavacca, and C. Chiastra, Med Eng Phys **75**, 23 (2020).

[40]   V. M. Pereira, O. Brina, A. Marcos Gonzales, A. P. Narata, P. Bijlenga, K. Schaller, K. O. Lovblad, and R. Ouared, J Biomech **46** (9), 1531 (2013).

[41]   K. R. Moyle, L. Antiga, and D. A. Steinman, J Biomech Eng **128** (3), 371 (2006).

[42]   I. C. Campbell, J. Ries, S. S. Dhawan, A. A. Quyyumi, W. R. Taylor, and J. N. Oshinski, J Biomech Eng **134** (5), 051001 (2012).

[43]   J. G. Myers, J. A. Moore, M. Ojha, K. W. Johnston, and C. R. Ethier, Ann Biomed Eng **29** (2), 109 (2001).

[44]   R. Ponzini, C. Vergara, G. Rizzo, A. Veneziani, A. Roghi, A. Vanzulli, O. Parodi, and A. Redaelli, IEEE Trans Biomed Eng **57** (7), 1807 (2010).

[45]   P. Xu, X. Liu, H. Zhang, D. Ghista, D. Zhang, C. Shi, and W. Huang, Biomech Model Mechanobiol **17** (6), 1581 (2018).

[46]   P. E. Gates, A. Gurung, L. Mazzaro, K. Aizawa, S. Elyas, W. D. Strain, A. C. Shore, and R. Shandas, Ultrasound Med Biol **44** (7), 1392 (2018).

[47]   J. B. Thomas, L. Antiga, S. L. Che, J. S. Milner, D. A. Steinman, J. D. Spence, B. K. Rutt, and D. A. Steinman, Stroke **36** (11), 2450 (2005).

[48]   F. K. Foster, P. M. Chikos, and J. S. Frazier, Journal of Clinical Ultrasound **13**, 385 (1985).

[49]   A. V. Kamenskiy, Pipinos, II, J. S. Carson, J. N. MacTaggart, and B. T. Baxter, J Vasc Surg **62** (6), 1521 (2015).

[50]   E. C. S. T. C. Group, The Lancet **351** (9113), 1379 (1998).

51   A. N. Nicolaides, S. K. Kakkos, E. Kyriacou, M. Griffin, M. Sabetai, D. J. Thomas, T. Tegos, G. Geroulakos, N. Labropoulos, C. J. Dore, T. P. Morris, R. Naylor, A. L. Abbott, S. Asymptomatic Carotid, and G. Risk of Stroke Study, J Vasc Surg **52** (6), 1486 (2010).

52   A. R. Naylor, P. M. Rothwell, and P. R. Bell, Eur J Vasc Endovasc Surg **26** (2), 115 (2003).

53   J. A. Deweese, A. G. May, E. O. Lipchick, and C. G. Rob, Stroke **1** (1970).

54   M. Lu, Y. Cui, P. Peng, H. Qiao, J. Cai, and X. Zhao, J Atheroscler Thromb **26** (8), 720 (2019).

55   N. Freidoonimehr, R. Chin, A. Zander, and M. Arjomandi, Physics of Fluids **33** (8) (2021).

56   A. Lauric, J. Hippelheuser, M. G. Safain, and A. M. Malek, J Biomech **47** (12), 3018 (2014).

57   C. G. Caro, D. J. Doorly, M. Tarnawski, K. T. Scott, Q. Long, and C. L. Dumoulin, in *Proceedings: Mathematical, Physical and Engineering Sciences* (The Royal Society, London, 1996), Vol. 452, pp. 185.

58   S. C. Nicholls, D. J. Phillips, J. F. Primozich, R. L. Lawerence, T. R. Kohler, T. G. Rudd, and E. Strandness, Stroke **20** (2) (1989).

59   H. Xiao and P. Cinnella, Progress in Aerospace Sciences **108**, 1 (2019).

60   P. A. Stonebridge, S. A. Suttie, R. Ross, and J. Dick, Eur J Vasc Endovasc Surg **52** (5), 674 (2016).

61   C. W. Kerber and D. Liepsch, American Journal of Neuroradiology **15**, 1065 (1994).

62   L. F. Valencia, J. Azencot, and M. Orkisz, in *Quinto Congreso Colombiano de Computación* (Bolivar, Colombia, 2010).

63   M. Samaee, A. Nooraeen, M. Tafazzoli-Shadpour, and H. Taghizadeh, Physics of Fluids **34** (7) (2022).

64   N. Kumar, S. M. A. Khader, R. Pai, S. H. Khan, and P. A. Kyriacou, International Journal of Engineering Science **154** (2020).

65   (ANSYS).

66   (ANSYS).

67   C. Sansour, International Journal of Solids and Structures **38**, 9221 (2001).

68   M. H. Amiri, A. Keshavarzi, A. Karimipour, M. Bahiraei, M. Goodarzi, and J. A. Esfahani, Heat and Mass Transfer **55** (7), 2037 (2019).

69   N. Kumar, R. Pai, M. S. Manjunath, A. Ganesha, and S. M. Abdul Khader, Journal of the Brazilian Society of Mechanical Sciences and Engineering **43** (8) (2021).

70   J. R. Womersely, Journal of Physiology **127**, 553 (1955).

71   J. Ryschlewski, Journal of Applied Mathematics and Mechanics **48** (3), 303 (1985).

[72]   ANSYS, (2009).

[73]   D. Gallo, P. B. Bijari, U. Morbiducci, Y. Qiao, Y. J. Xie, M. Etesami, D. Habets, E. G. Lakatta, B. A. Wasserman, and D. A. Steinman, J R Soc Interface **15** (147) (2018).

[74]   M. T. Ngo, H. S. Kwak, G. Ho Chung, and E. J. Koh, Vascular **27** (3), 312 (2019).

[75]   M. Apaydin and K. Cetinoglu, Clinical Imaging **70**, 10 (2021).

[76]   C. C. Mei and H. Jing, Math Biosci **280**, 62 (2016).

[77]   A. M. Moerman, S. Korteland, K. Dilba, K. van Gaalen, D. H. J. Poot, A. van Der Lugt, H. J. M. Verhagen, J. J. Wentzel, A. F. W. van Der Steen, F. J. H. Gijsen, and K. Van der Heiden, Front Bioeng Biotechnol **9**, 828577 (2021).

[78]   M. Albadawi, Y. Abuouf, S. Elsagheer, S. Ookawara, and M. Ahmed, Physics of Fluids **33** (12) (2021).

[79]   P. Eshtehardi, A. J. Brown, A. Bhargava, C. Costopoulos, O. Y. Hung, M. T. Corban, H. Hosseini, B. D. Gogas, D. P. Giddens, and H. Samady, Int J Cardiovasc Imaging **33** (7), 1089 (2017).

[80]   P. Libby, G. Pasterkamp, F. Crea, and I. K. Jang, Circ Res **124** (1), 150 (2019).

[81]   Y. Chen, X. Yang, A. J. Iskander, and P. Wang, Physics of Fluids **32**, 101902 (2020).

[82]   L. Lan, H. Liu, V. Ip, Y. Soo, J. Abrigo, F. Fan, S. H. Ma, K. Ma, B. Ip, J. Liu, Y. Fan, J. Zeng, V. Mok, L. Wong, D. Liebeskind, T. Leung, and X. Leng, Stroke **51** (10), 3064 (2020).

[83]   A. Bantwal, A. Singh, A. R. Menon, and N. Kumar, Journal of Fluids Engineering **144** (2) (2022).

[84]   D. Lopes, H. Puga, J. Teixeira, and R. Lima, J Biomech **111**, 110019 (2020).